JCB Journal of Cell Biology

TOOLS

Volumetric morphometry reveals spindle width as the best predictor of mammalian spindle scaling

Tobias Kletter[1], Sebastian Reusch[1], Tommaso Cavazza[2], Nils Dempewolf[3], Christian Tischer[4], and Simone Reber[1,3]

The function of cellular structures at the mesoscale is dependent on their geometry and proportionality to cell size. The mitotic spindle is a good example why length and shape of intracellular organelles matter. Spindle length determines the distance over which chromosomes will segregate, and spindle shape ensures bipolarity. While we still lack a systematic and quantitative understanding of subcellular morphology, new imaging techniques and volumetric data analysis promise novel insights into scaling relations across different species. Here, we introduce Spindle3D, an open-source plug-in that allows for the quantitative, consistent, and automated analysis of 3D fluorescent data of spindles and chromatin. We systematically analyze different mammalian cell types, including somatic cells, stem cells, and one- and two-cell embryos, to derive volumetric relations of spindle, chromatin, and the cell. Taken together, our data indicate that mitotic spindle width is a robust indicator of spindle volume, which correlates linearly with chromatin and cell volume both within single cell types and across mammalian species.

Introduction

Size and shape in general are important biological features. Classically, morphometrics have been performed on the level of organisms, tissues, and cells. Now, the continuous improvement of imaging techniques and data analysis allows for the accurate measurement of organelle geometry at the micrometer scale and thus enables the development of quantitative scaling laws at the mesoscale.

Anecdotal evidence suggested that spindle length scaled with cell size. More recent studies, however, show that the nature of spindle scaling and size control is more complex. In different cells, spindle length spans over an order of magnitude, and various molecular scaling mechanisms are likely to contribute to different degrees to cover the entire length regime (Rieckhoff et al., 2020). For example, the length of mitotic spindles increases with cell length in small cells, but in very large cells, spindle length approaches an upper limit (Wühr et al., 2008; Courtois et al., 2012; Lacroix et al., 2018; Rieckhoff et al., 2020). More precisely, spindle length scales linearly with cytoplasmic volume (Hazel et al., 2013; Good et al., 2013). Further, spindle size needs to be coordinated with chromosome dimensions, a fact that is established (Mora-Bermúdez et al., 2007; Lipp et al., 2007; Dinarina et al., 2009; Kieserman and Heald, 2011) but poorly understood. All the above observations point to an important (and in some cases still open) question: What are the relevant morphometric measures to precisely formulate spindle scaling phenomena?

While most experimental studies still measure spindle length and cell diameter or collapse them into area information, theoretical arguments regularly use volumetric data (Good et al., 2013; Reber et al., 2013; Rieckhoff et al., 2020). Previous work has analyzed spindles in 3D (Dumont and Mitchison, 2009; Takagi et al., 2013; Reber et al., 2013; Takagi et al., 2014; Baran et al., 2016; Oh et al., 2016; Cai et al., 2018, So et al., 2019; Rieckhoff et al., 2020, Schneider et al., 2021), but there is still no standard or automated open-source tool for analyzing spindle morphometrics. Tools available for analyzing spindle size and geometry so far only allow for 2D analysis (Crowder et al., 2015; Grenfell et al., 2016). Here, we show that spindle parameters differ significantly when measured in 2D as compared with 3D; they are thus error prone and might lead to incorrect mechanistic conclusions. We argue that quantitative measurements from 3D datasets are essential to allow for accurate mechanistic interpretation and derive conceptual scaling laws. Therefore, we use quantitative microscopy, together with a newly developed analysis tool, Spindle3D, and the segmentation software Ilastik (Berg et al., 2019), to derive quantitative 3D morphometry data

---

[1]Integrative Research Institute Life Sciences, Humboldt-Universität zu Berlin, Berlin, Germany; [2]Department of Meiosis, Max Planck Institute for Biophysical Chemistry, Göttingen, Germany; [3]University of Applied Sciences Berlin, Berlin, Germany; [4]Advanced Light Microscopy Facility, European Molecular Biology Laboratory, Heidelberg, Germany.

Correspondence to Simone Reber: simone.reber@iri-lifesciences.de.

https://doi.org/10.1083/jcb.202106170

on spindle, chromatin, and cell volume. Spindle3D is available as a free and open-source plug-in (https://sites.imagej.net/Spindle3D) in Fiji (Schindelin et al., 2012) and allows for the quantitative, consistent, and automated analysis of 3D fluorescent data of spindles and chromatin. Our analysis of a variety of cell types proves the robustness of the Spindle3D plug-in, which thus can be broadly used by researchers to inform future biological and physical concepts of spindle scaling and size control across many experimental systems.

Results

3D analysis of fluorescent spindle and chromatin data allows for the accurate extraction of quantitative morphometric parameters

To extract quantitative parameters of spindle and chromatin morphometries, our plug-in requires a two-channel Z-series with fluorescent tubulin and chromatin labeling (Figs. 1 A and S1) as a minimum input, which allows for object detection and spindle axis localization (Materials and methods). Classically, spindle length is defined as the pole-to-pole distance. Consistently, we first define the spindle axis, along which spindle length is specified, as the distance between the two spindle poles (Fig. 1 B). Next, spindle width is measured orthogonally to the spindle axis and reflects the diameter of the spindle ellipsoid at its equator. The volumes of all voxels within the segmented spindle mask add up to yield a spindle's volume. As the orientation of the mitotic spindle can determine both the relative size and the position of the daughter cells (as reviewed in McNally, 2013), we provide a measure for the spindle angle, which describes the tilt of the spindle axis relative to the reference plane. Chromatin can induce spindle assembly (Heald et al., 1996) and influences the spindle's geometry (Dinarina et al., 2009). Hence, we use the intensity profile of the chromatin to measure the metaphase plate, which expands orthogonally to the determined spindle axis (Fig. S1 A). We define the metaphase plate width as the extent of chromatin along its shortest axis and the metaphase plate length as the mean chromatin diameter. Again, the volumes of all voxels within the segmented chromatin mask add up to yield chromatin volume. In some cell types, we consistently find the chromosomes aligned with a central opening in the metaphase plate, a phenomenon we termed chromatin dilation, which is measured using a radial intensity profile (Figs. 1 B and S1 B).

By projecting our 3D microscopic images into 2D planes (Fig. 1 C), we identified and quantified potential sources of error when spindle parameters are only analyzed in two dimensions. Collapsing 3D into 2D information resulted in the distortion of morphometric parameters. The error is particularly evident when spindles are not perfectly parallel to the substrate but tilted in Z (Fig. 1 D). As a consequence, axial extents such as spindle length and metaphase plate width will be under- or overestimated, respectively. Even moderate spindle angles of 25° produce measurement errors of ~12.5% (Fig. 1 D). Furthermore, because spindle morphologies are not always perfectly symmetrical, information on spindle width and metaphase plate length are lost in 2D projections. Taken together, we recommend the acquisition and analysis of 3D datasets, which is essential to derive accurate quantitative measurements, in particular if they shall inform mathematical models.

Spindle3D robustly derives morphometric parameters across a variety of cell types and phyla

To allow for an automated and quantitative analysis of spindle and chromatin parameters, we developed a 3D morphometric analysis workflow (Fig. S1). To demonstrate its applicability and robustness, we subjected confocal images of live metaphase spindles from wild-type HEK293 cells (*Homo sapiens*), a HeLa Kyoto cell line (*H. sapiens*), Ptk$_2$ cells (*Potorous tridactylis*), bovine one- and two-cell embryos (*Bos taurus*), and mouse embryonic stem cells (mESCs; *Mus musculus*) to our 3D morphometric analysis (Fig. 2 A). The workflow produced segmented outputs with spindle axis–aligned voxel coordinates (Fig. 2 B). Analyzed spindle lengths ranged from 8.5 to 27.0 µm (Fig. 2 C). Together with mESCs, the two human cell lines (HEK293 and HeLa Kyoto) showed spindles of comparable lengths (11.5 ± 1.2 µm [mean ± SD], 11.5 ± 1.4 µm, and 13.6 ± 2.0 µm, respectively), contrasted by the considerably longer spindles of the bovine one- and two-cell embryos and Ptk$_2$ cells with an average length of 18.1 ± 2.4 µm, 17.6 ± 2.3 µm, and 16.3 ± 3.2 µm, respectively. However, together with mESCs, Ptk$_2$ cells displayed narrower spindles (Fig. 2 D), producing markedly increased spindle aspect ratios (Fig. 2 E), a shape descriptor defined as the ratio of spindle length and width. We found that small aspect ratios often coincided with flat spindle poles, while spindles with large aspect ratios had visibly pointed poles. Of the datasets tested, bovine one- and two-cell embryos harbored spindles with the largest volumes (Fig. 2 F) of 1,911.6 ± 450.9 µm^3 (mean ± SD) and 1,796.0 ± 427.8 µm^3, respectively, consistent with spindles reaching an upper limit in early development (Wühr et al., 2008; see Discussion). In contrast, spindles in mESCs occupied only a fraction of this volume (408.8 ± 101.6 µm^3). Independent of cell type, the majority of spindles showed tilted angles (Fig. 2 G) that fall within a range of 0 to 77°, highlighting the importance of 3D analysis. Intriguingly, the volume and length of the metaphase plate (Fig. 2, H and I) did not reflect cell type–specific genome sizes or chromosome numbers (Fig. S2, A–F), hinting toward different levels of chromatin compaction (as reviewed in Levy and Heald, 2012). In addition, our analysis quantified various levels of chromatin dilation. Especially in mESCs spindles (but also in a large fraction of the HeLa Kyoto population), chromatin plates were frequently and considerably dilated (chromatin dilation >0.5; Fig. 2 J). Taken together, the 3D analysis workflow provided by our plug-in robustly revealed cell type–specific spindle and chromatin morphology across different cell lines.

Fixation and sample preparation alter spindle and chromatin morphology

In our explorations, we frequently observed a discrepancy in spindle sizes of live cells compared with cells that were fixed and mounted on cover slides. To systematically test the influence of fixation and mounting, we used HeLa Kyoto cells and mESCs stably expressing tubulin-GFP, allowing us to directly benchmark the mounted cells to their live counterparts (Fig. 3, A and

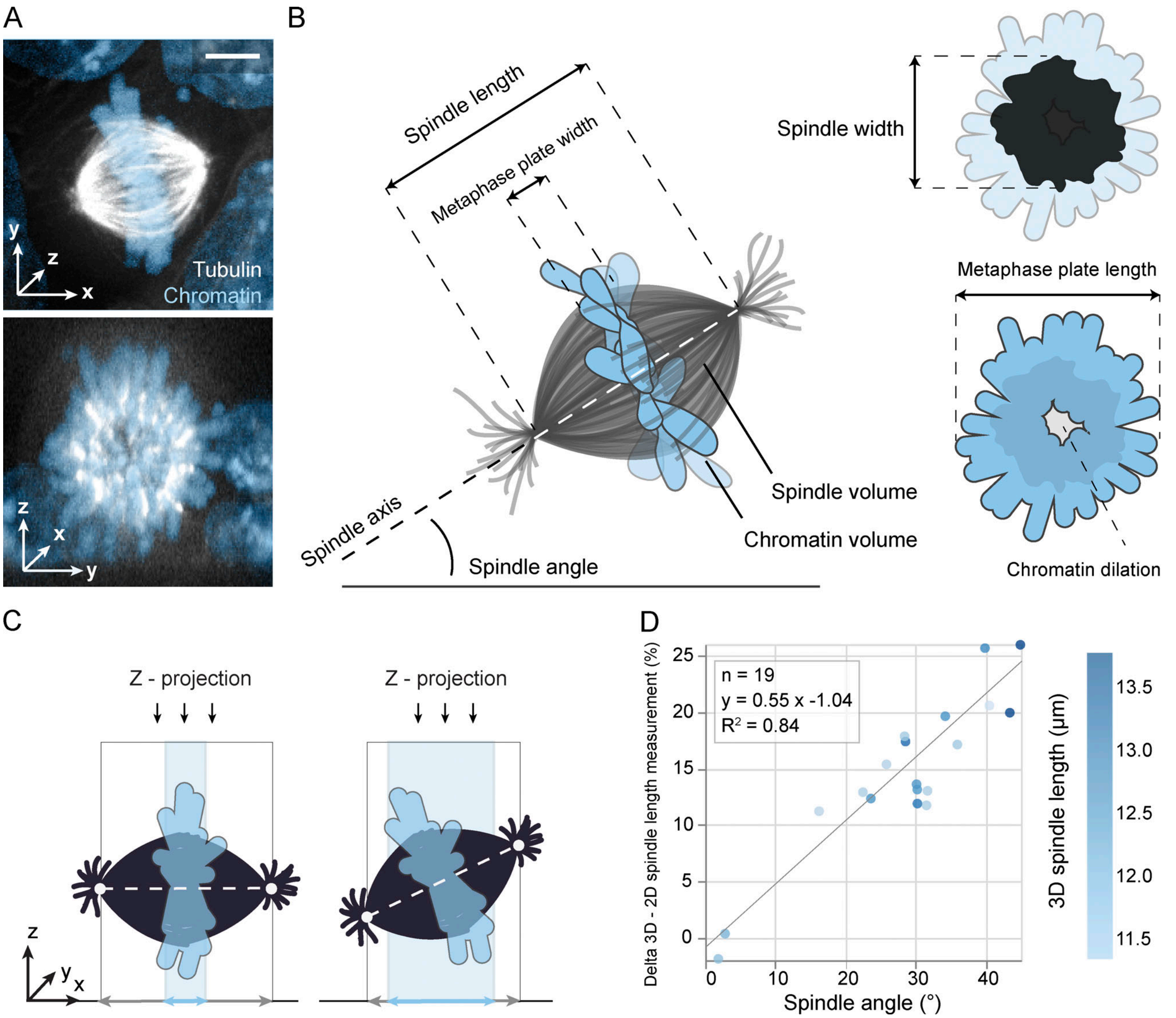

Figure 1. **3D analysis of fluorescent spindle and chromatin data allows for the accurate extraction of morphometric parameters.** **(A)** Top: Projected micrograph of a mitotic mouse embryonic stem cell expressing tubulin-GFP (white); DNA is stained with Hoechst (blue). Bottom: Same image resliced to display the equatorial section of the spindle. Scale bar, 5 µm. **(B)** Schematic of a mitotic spindle and its relevant morphometric parameters extracted by Spindle3D. Along the spindle axis, Spindle3D measures spindle length and metaphase plate width, and in the lateral direction, it measures spindle width and metaphase plate length. Chromatin dilation quantifies the central signal strength of the metaphase plate. **(C)** Morphometry on projected spindles distorts measurements if spindle axes are tilted. **(D)** The relationship between the spindle angle and the percent discrepancy between the 2D (projected) and 3D spindle length quantification (*n* = 19). Circles represent individual spindles, and color is coded according to 3D spindle length. Line shows linear regression.

B). Additionally, we measured cells that were chemically fixed, but not mounted. Using our plug-in, morphometric analysis revealed a marked decrease in spindle volumes in cells that were fixed and mounted in mounting media (Fig. 3 C). In addition, we frequently observed deformed spindle shapes in these samples with shifted aspect ratios (Fig. 3 D). When samples were fixed, but not mounted, spindle volumes were comparable to live spindles (Fig. 3 C). In these samples, as well as in the fixed and mounted samples, we observed a distorted volumetric relationship between spindle and chromatin (Fig. 3 E). Taken together, we show that sample preparation may induce artifacts in spindle and chromatin morphology and should be considered with great care. Importantly, as the introduced errors are not isotropic, such analyses may distort geometrical relationships and thus lead to error-prone scaling relations. Therefore, we recommend using live cells where possible, and for assays with fixed samples (e.g., immunofluorescence), we suggest refraining from mounting samples.

In mammalian cells, spindle width reflects spindle volume

Several lines of evidence imply that there are correlations among chromatin dimensions, spindle geometry, and steady-state microtubule polymer mass (as reviewed in Levy and Heald, 2012). From our analyses, we can now establish such simple scaling relations. We first explored the relationship between the length of the spindle and its volume (Fig. 4 A) and

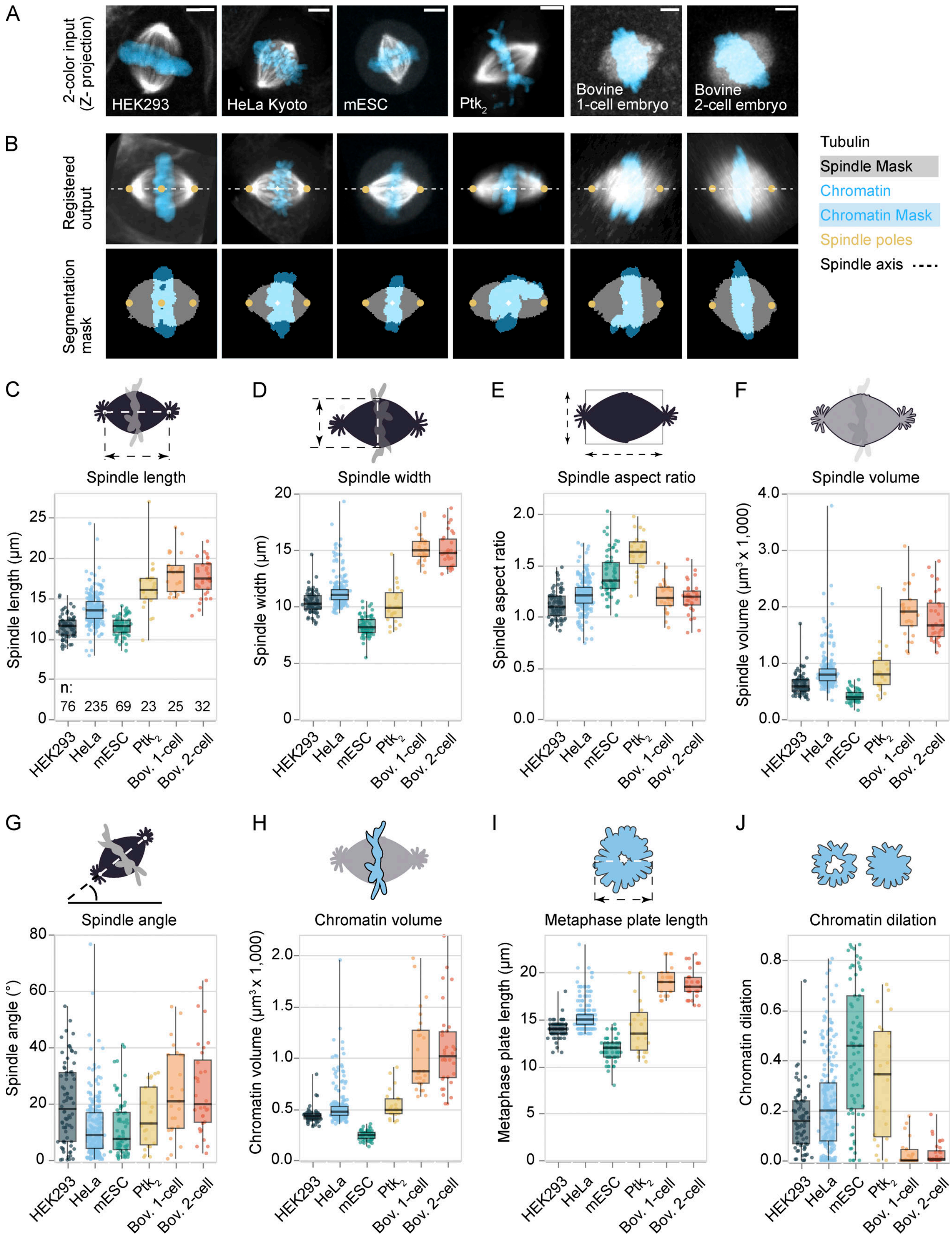

Figure 2. **Spindle3D robustly derives morphometric parameters across a variety of cell types. (A)** Representative live fluorescent 3D spindle datasets (maximum-projected) from different cells expressing labeled tubulin or microtubule-associated proteins or treated with SiR-tubulin (white). Chromatin (blue) is visualized with Hoechst, SiR-DNA, or H2B-mScarlet. Scale bars, 5 µm. **(B)** Automated axial registration and segmentation of two-color (tubulin grayscale,

chromatin blue) input images as shown in A. Spindle3D exports axially aligned output images containing segmentation masks and spindle pole localization for quality control. **(C–J)** Quantification of spindle length (C), spindle width (D), spindle aspect ratio (E), spindle volume (F), spindle angle (G), chromatin volume (H), metaphase plate length (I), and chromatin dilation (J) for all cell types. Circles are individual data points and represent a single spindle measurement (HEK293, *n* = 76; HeLa Kyoto, *n* = 235; mESCs, *n* = 69; Ptk$_2$, *n* = 23; bovine one cell, *n* = 25; bovine two cell, *n* = 32). Boxes describe the interquartile range, horizontal lines in the box denote the median, and whiskers show minimum and maximum.

---

between the width of the spindle and its volume (Fig. 4 B). When calculating the Spearman correlation coefficients (r_s), we found a stronger correlation between spindle width and spindle volume ($r_s = 0.93$, $P = 7 \times 10^{-205}$; Fig. 4 B) than between spindle length and spindle volume ($r_s = 0.82$, $P = 2 \times 10^{-113}$; Fig. 4 A). This also held true when looking at the individual cell types (Fig. 4, A and B). As this was unexpected, we first verified manually that spindle length and width were represented reliably by our

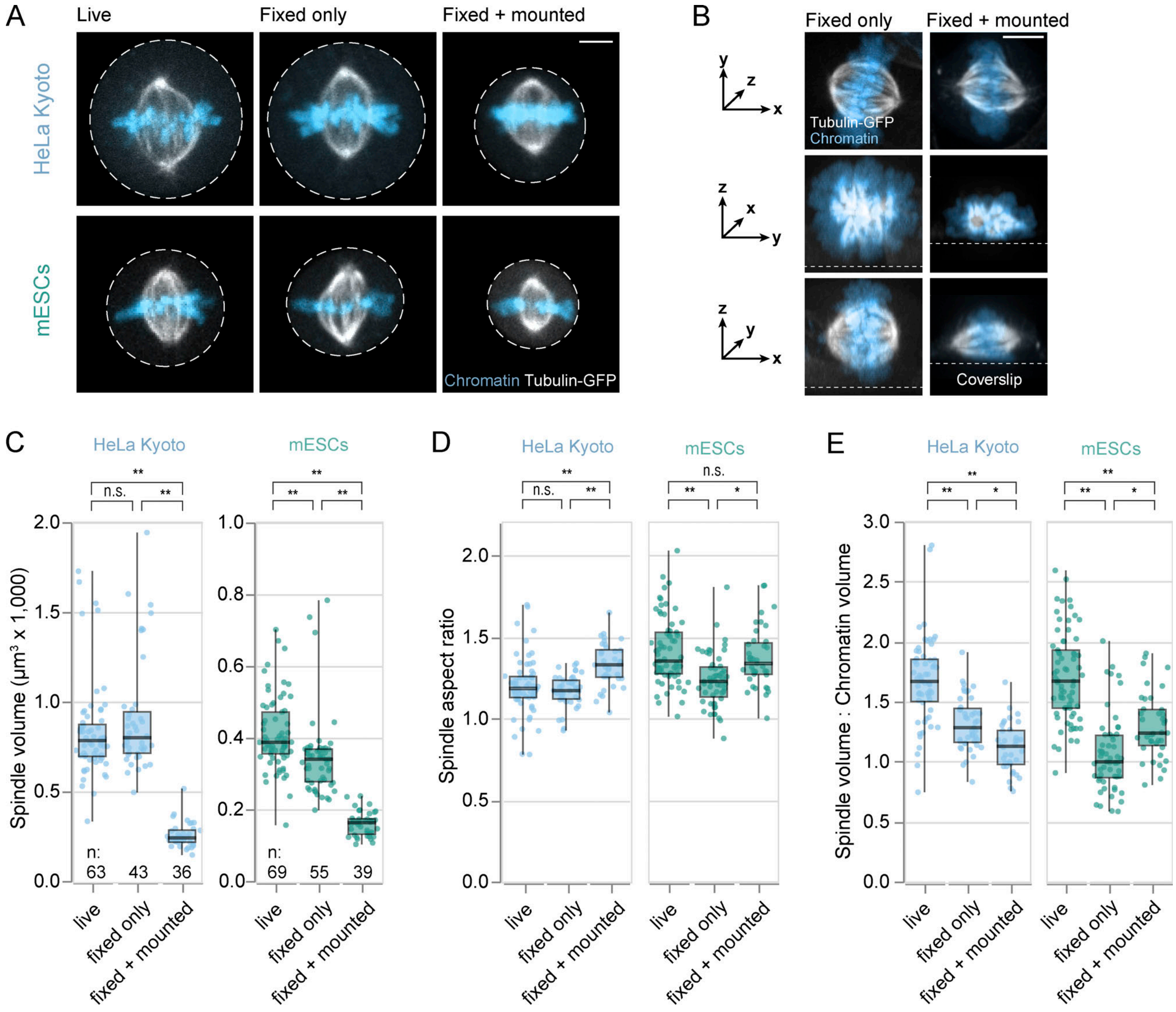

Figure 3. **Sample preparation alters spindle and chromatin morphology. (A)** Fluorescently tagged tubulin allows for direct comparison of spindle morphology in live and fixed specimens. Left column shows representative mitotic cells (HeLa Kyoto and mESCs lines both stably expressing tubulin-GFP) when imaged live. Cells depicted in the central column were chemically fixed before imaging. Cells in the right column were fixed and embedded in mounting media. Tubulin-GFP signal is in white, and DNA is shown in blue. Dotted lines indicate cell boundaries. Scale bar, 5 µm. **(B)** Left column shows projections along the imaging axis (top), x axis (middle), and y axis (bottom) of a chemically fixed mESC imaged in 1× PBS. Analogously, the right column shows an mESC that was fixed and mounted. Colors as in A. The dotted lines indicate the plane of the cover glass. Scale bar, 5 µm. **(C–E)** Fixation and sample preparation introduce artifacts to morphometric parameters such as spindle volume (C) and thus distort geometrical relationships among spindle measures such as spindle aspect ratio (D) and the ratio of spindle volume to chromatin volume (E). Circles represent individual spindles (HeLa Kyoto live, *n* = 63; HeLa Kyoto fixed, *n* = 43; HeLa Kyoto fixed + mounted, *n* = 36; mESCs live, *n* = 69; mESCs fixed, *n* = 55; mESCs fixed + mounted, *n* = 39). Boxes denote interquartile range, and horizontal lines show medians. Whiskers show minimum and maximum. P values from ANOVA with Tukey's test as post-hoc analysis. *, P < 0.05; **, P = 0.001; n.s., not significant (P > 0.05).

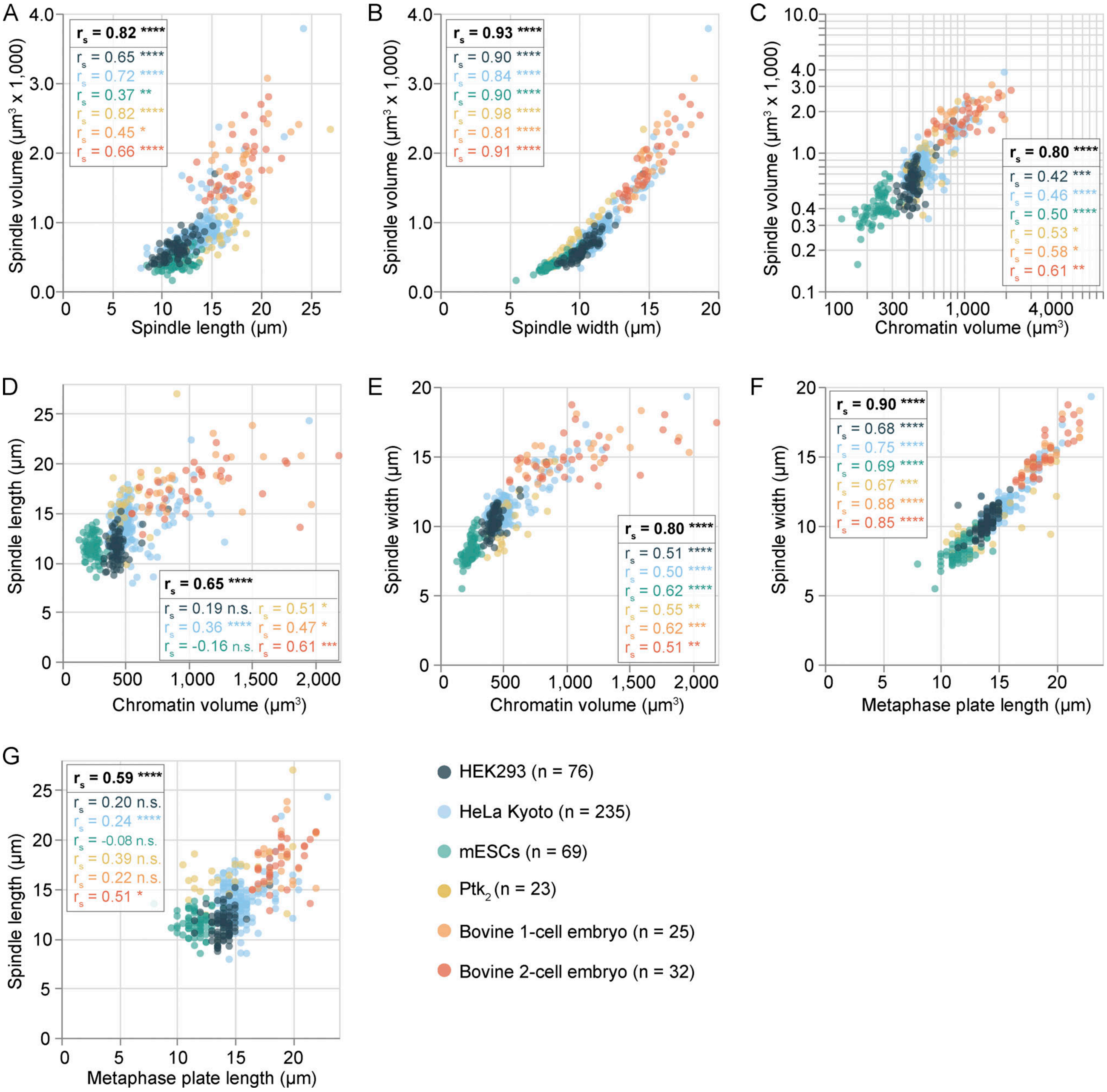

Figure 4. **In mammalian cells, spindle width, rather than spindle length, reflects spindle volume. (A and B)** Relationship between spindle length and spindle volume (A) and spindle width and spindle volume (B) in live spindles of five different cell types. **(C)** Volumetric relationship between chromatin and spindle. **(D and E)** Relationship between chromatin volume and spindle length (D) and chromatin volume and spindle width (E). **(F and G)** Relationship between metaphase plate length and spindle width (F) and metaphase plate length and spindle length (G). Circles represent individual spindles (HEK293, *n* = 76; HeLa Kyoto, *n* = 235; mESCs, *n* = 69; Ptk$_2$, *n* = 23; bovine one cell, *n* = 25; bovine two cell, *n* = 32). r_s, Spearman correlation coefficient; black coefficients show correlation for pooled data (*n* = 460), and colored coefficients show cell-type resolved correlations. *, P < 0.05; **, P < 0.005; ***, P < 0.001; ****, P < 0.0001; n.s., P > 0.05.

automated measurements (Fig. S3, A–D). Because spindle width varies at the equator, we can measure spindle width as the average extent of the spindle mask projected along the spindle axis (Figs. 4 B and S1 C) or as the maximum or minimum spindle width (Fig. S3 E). In either case, spindle width yielded strong correlations with spindle volume (Fig. S3, F and G). Chromatin has been shown to affect both spindle length and shape (Dinarina et al., 2009; Hara and Kimura, 2013). We thus plotted spindle volume as a function of chromatin volume (Fig. 4 C), which we find to correlate linearly ($r_s = 0.80$, $P = 3 \times 10^{-103}$). This is surprising, because in embryonic systems, varying chromatin content had a weak effect on spindle size, while varying chromatin geometry influenced spindle assembly more drastically (Brown et al., 2007; Wühr et al., 2008; Dinarina et al., 2009). We therefore plotted spindle length and width against chromatin volume and again found that spindle width correlated more strongly with chromatin volume (r_s = 0.65, P = 3 × 10^{-56} for spindle length; Fig. 4 D; and r_s = 0.80, P = 10^{-105} for spindle width; Fig. 4 E). Previous data implied that symmetric and thus functional spindles only self-organize around specific chromatin dimensions (Dinarina et al., 2009). Indeed, we find an almost perfect linear relation between spindle width and the length of the metaphase plate (r_s = 0.90, P = 5 × 10^{-163}; Fig. 4 F), while spindle length and metaphase plate length only showed moderate dependencies (r_s = 0.59, P = 9 × 10^{-44}; Fig. 4 G). Taken together, we show that for the size regime investigated, steady-state spindle width, rather than spindle length, is a reliable predictor of overall spindle volume.

Spindle volume and chromatin volume scale linearly with cell volume

In many systems, cell or cytoplasmic volume is a major determinant of spindle size (Good et al., 2013; Hazel et al., 2013; Farhadifar et al., 2015; Wang et al., 2016; Lacroix et al., 2018). So, to reliably measure cell volume, we took advantage of the fact that mitotic cells expressing fluorescently tagged tubulin show, next to the prominent spindle signal, distinctive fluorescence of soluble tubulin throughout the cytoplasm (Fig. 5 A). We thus used pixel classification–based 3D segmentation (Berg et al., 2019) of mitotic cells expressing fluorescent tubulin as a readout of cell volume and cell sphericity to complement the morphometric data generated by our plug-in. Based on this, we trained random forest classifiers to distinguish and predict mitotic cell volumes (Fig. 5 B) and verified that this approach was as accurate as manual volumetric segmentations guided by cell membrane labeling (Fig. S4, A–C). We live imaged and analyzed HeLa Kyoto cells, mESCs, and Ptk_2 cells expressing fluorescently tagged tubulin. With average cell volumes of ∼6,100 µm^3 (HeLa Kyoto cells; Fig. 5 C), 2,850 µm^3 (mESCs), and 7,450 µm^3 (Ptk_2 cells), all three cell types displayed volumetric scaling between the cell and the respective spindle (r_s = 0.86, P = 6 × 10^{-56}; Fig. 5 D). We measured spindle volume as the total volume of all voxels within the segmented spindle mask; however, spindle volume might vary considerably from spindle mass (defined as the total steady-state microtubule polymer mass; Reber et al., 2013) depending on microtubule density and spindle architecture. We therefore quantified steady-state spindle mass using Spindle3D in conjunction with the cell volume masks (Fig. 5 E). For all three cell types examined, spindle mass was directly proportional to spindle volume (r_s = 0.94, P = 3 × 10^{-87}; Fig. S5 A) and displayed a comparable scaling relation with cell volume (r_s = 0.93, P = 3 × 10^{-82}; Fig. 5 F). Recurrently, spindle width, rather than spindle length, correlated with spindle mass (Fig. S5, B and C). When evaluating dimensional scaling, spindle length displayed a considerable association with cell volume (r_s = 0.75, P = 5 × 10^{-35}; Fig. 5 G), but with notably poorer correlation in mESCs (r_s = 0.18, P = 0.16), while spindle width robustly scaled with cell volume (r_s = 0.80, P = 6 × 10^{-43}; Fig. 5 H) in all three cell lines. Interestingly, cells exerted a cell type–specific spindle size specification. While spindle volumes in both HeLa cells and mESCs occupied ∼14% of total cell volume, it was only 11% in Ptk_2 cells (Fig. 5 I). We reasoned that Ptk_2 spindles might be more densely packed. However, we found that the average tubulin (polymer and free) densities within the spindles were comparable among the three cell types (Fig. S5 D) and that Ptk_2 cells indeed partitioned less of the total cellular tubulin to their spindles than the other two cell types (Fig. S5 E). In contrast to the other two cell lines, Ptk_2 cells do not round up during mitosis (Fig. 5 J). As a consequence, they show an increased cell surface area to cell volume ratio (CA/CV) at a given cell volume (Fig. S5 F). Based on reports that spindle scaling can be physically linked to changes in CA/CV (Brownlee and Heald, 2019; Rieckhoff et al., 2020), we asked whether CA/CV provided an explanation for the unique scaling behavior of Ptk_2 cells. When plotting spindle mass against CA/CV, Ptk_2 cells lost all significant correlation (r_s = −0.20, P = 0.39; Fig. 5 K). Similarly, CA/CV showed comparably weak association with the geometrical parameters of Ptk_2 spindles (Fig. S5, G and H). Finally, we found chromatin volume to linearly scale with cell volume (r_s = 0.88, P = 2 × 10^{-61}; Fig. 5 L). However, our current understanding of mitotic chromosome scaling with cell volume is so far limited to a single candidate mechanism, chromatin packing density (as reviewed in Heald and Gibeaux, 2018). While studies in *Xenopus* and *Caenorhabditis elegans* show that mitotic chromosome size decreases throughout embryogenesis (Hara et al., 2013; Ladouceur et al., 2015; Kieserman and Heald, 2011), systematic and quantitative data from somatic cells are missing. Taken together, our 3D spindle morphometry revealed that spindle volume and mass scale linearly with chromatin volume (but not chromosome number or genome size) and cell volume. Intriguingly, in terms of the spindle's spatial dimensions, it was not spindle length but rather spindle width that revealed a robust correlation with chromatin and cell volume. Future work will build on our size scaling analyses to decipher the molecular mechanisms that drive spindle scaling and size control in different species and during development.

Discussion

So far, early embryonic development, in particular of frogs, fish, and worms (Wühr et al., 2008; Hara and Kimura, 2009; Wilbur and Heald, 2013; Rieckhoff et al., 2020), has provided experimental models to study spindle scaling and size control. One advantage of early embryonic development is the rapid and dramatic decrease in cell volume over several orders of magnitude. In contrast, somatic cells only show a small variation in cell volume for a given cell type, which makes it harder to discover potential scaling regimes (Marshall, 2020). Here, we use volumetric fluorescent microscopy data from somatic cells, stem cells, and one- and two-cell embryos as well as cells that round up during mitosis or are naturally flat to systematically study scaling relations of spindle, chromatin, and cell geometry. Our data on bovine one- and two-cell embryos imply that the linear scaling regimes defined so far (cell volume [V_c] <10^6 µm^3; Rieckhoff et al., 2020; and cell diameter [d_c] <140 µm; Crowder et al., 2015) might not be universal. Although bovine one-cell embryos measure 117.5 ± 5.9 µm in diameter (Fig. S4 D) and thus are well within the linear scaling regimen of d_c < 140 µm, spindles do not significantly reduce in size from the one-cell (18.1 ± 2.4 µm) to two-cell embryo (17.6 ± 2.3 µm). Boundaries

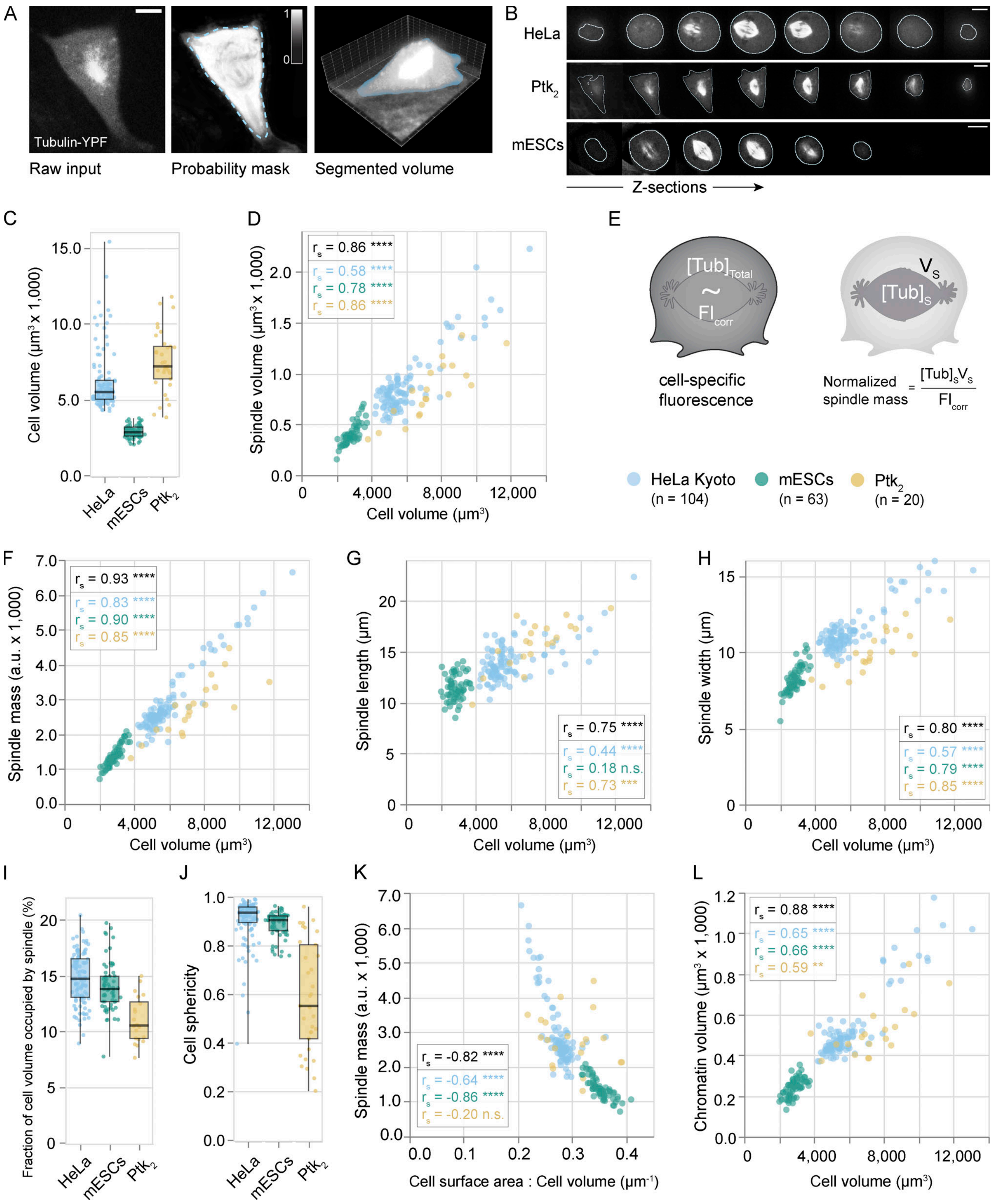

Figure 5. **Spindle volume and chromatin volume scale linearly with cell volume. (A)** Rationale for quantifying cell volume via cytoplasmic tubulin fluorescence by pixel classification in the segmentation software Ilastik (Berg et al., 2019). Voxels of input micrographs (left) were converted to probabilities for mitotic cytoplasm (center). Probability masks were thresholded at 0.5 (dotted line) to produce the final volume mask (blue, right). Scale bar, 5 µm. **(B)** Z-series showing the cell boundaries (blue) as determined by pixel classification in three cell lines expressing fluorescent tubulin. Scale bars, 5 µm. **(C)** Distributions of cell volumes in three cell lines. **(D)** Bivariate relationships between cell volume and spindle volume. **(E)** Quantifying spindle mass as the polymer and free tubulin mass within the spindle volume (V_s), normalized by a cell-specific fluorescence correction factor (FI_{corr}) proportional to the total fluorescent tubulin concentration ($[Tub]_{Total}$). $[Tub]_S$, tubulin concentration within spindle volume (Materials and methods). **(F–H)** Bivariate relationships between cell volume and

spindle mass (F), cell volume and spindle length (G), and cell volume and spindle width (H). **(I)** Distributions of cell sphericity in three cell lines. **(J)** Distributions showing the fraction of cell volume occupied by the spindle. **(K)** Relationship between the cell surface area: volume ratio and spindle mass. **(L)** Volumetric relationship between cell and chromatin. Circles reflect individual cells (HeLa Kyoto, $n = 104$. mESCs, $n = 63$. Ptk$_2$: $n = 20$). r_s, Spearman correlation coefficient; black coefficients show correlation for pooled data, and colored coefficients show cell-type resolved correlations. **, $P < 0.005$; ***, $P < 0.001$; ****, $P < 0.0001$; n.s., $P > 0.05$. Boxes denote interquartile range, horizontal lines represent medians, and whiskers show minimum and maximum.

of the linear scaling regime might be affected by species-specific cytoplasmic factors (Wilbur and Heald, 2013; Brownlee and Heald, 2019; Hirst et al., 2020). Furthermore, whereas it is commonly assumed that spindle length must be tightly tailored to the cell's dimensions to safeguard fidelity of chromosome segregation and cytokinesis (Goshima and Scholey, 2010; Reber and Hyman, 2015; Reber and Goehring, 2015), we observed that spindle length was loosely correlated with spindle, chromatin, and cell geometry. Instead, for the cell size regime and cell types investigated in this study, we found the width of the spindle to be a robust predictor of both spindle volume and mass and to correlate with cell and chromatin dimensions. It will be interesting to investigate in future work whether our findings also apply to other species and cell size regimes.

While chromatin is sufficient to induce spindle assembly (Heald et al., 1996), it remains unclear how its volume, surface area, or dimensions (or a combination of these factors) influence spindle assembly and geometry. In embryonic systems, chromatin content has been shown to have only a minor effect on spindle size. Therefore, it has been suggested that chromatin surface rather than chromatin volume or mass influences spindle size (Brown et al., 2007; Wühr et al., 2008; Dinarina et al., 2009). This is because chromatin triggers spindle self-organization via a diffusion-limited RanGTP gradient, which promotes microtubule nucleation and growth (Gruss et al., 2001). The spatial regulation of microtubule nucleation has recently been shown to determine the upper limit of spindle length (Decker et al., 2018), and particularly in large cells, spindle scaling has been suggested to be governed by microtubule nucleation (Rieckhoff et al., 2020). Chromosomal nucleation, however, might be more relevant in early embryonic systems than in somatic cells (Bird and Hyman, 2008; Cavazza et al., 2016). Furthermore, a combination of modeling and perturbation studies has shown that spindle length is insensitive to the length scale of the Ran gradient in human tissue culture cells (Oh et al., 2016). Thus, how chromatin and the Ran gradient influence microtubule nucleation and dynamics in different scaling regimes remains an exciting open question for future research.

Materials and methods

Antibodies

The antibodies used were anti-γ-tubulin (mouse, T6557; Sigma) and anti-mouse Alexa Fluor 568 (rabbit, A-11061; Thermo Fisher Scientific).

Plasmids and mRNA synthesis

The plasmids used were pEGFP-C1-mCherry-CaaX (based on Müller, 2020), mClover3-MAP4-MTBD (So et al., 2019), and H2B-mScarlet (So et al., 2019).

All mRNAs were synthesized using HiScribe T7 ARCA mRNA Kit (E2065S; New England Biolabs) following the manufacturer's protocol and quantified using the Qubit RNA HS Assay Kit (Q32852; Thermo Fisher Scientific).

Cell lines

The cell lines used included HeLa Kyoto and R1/E mESCs (gifts from Hyman laboratory, Max Planck Institute of Molecular Cell Biology and Genetics, Dresden, Germany), HEK293 (gift from Beckman laboratory, IRI Life Sciences, Berlin, Germany), and Ptk$_2$ (gift from Simons laboratory, Max Planck Institute of Molecular Cell Biology and Genetics, Dresden, Germany).

Mammalian tissue culture

R1/E mESCs were cultured in DMEM (high glucose, pyruvate; Gibco) supplemented with 16% FBS (Gibco), antibiotic–antimycotic (Invitrogen), nonessential amino acids (Gibco), β-mercaptoethanol (Gibco), and recombinant mouse leukemia inhibitory factor (ESGRO). For routine culturing, cells were passaged every 48 h and seeded at a density of 35,000 cells/cm^2 onto gelatin-coated dishes. HeLa Kyoto, HEK293, and Ptk$_2$ cell lines were cultured in DMEM (high glucose, pyruvate) supplemented with 10% FBS and antibiotic–antimycotic (Invitrogen) and passaged routinely. Prior to imaging, cells were seeded onto wells of 4-well imaging dishes (Ibidi) or 24-well imaging dishes (Ibidi). To support growth in adherent monolayer, mESCs were seeded onto wells coated with 5 μg/ml laminin-511 (BioLamina) in 1× PBS (supplemented with Ca^{2+} and Mg^{2+}). All cells were maintained at 37°C and 5% CO$_2$.

Transfection of HeLa Kyoto cells was performed using Lipofectamine 3000 (Thermo Fisher Scientific) according to the manufacturer's instructions.

Chemical fixation and immunostaining of tissue culture cells

For chemical fixation, R1/E mESCs and HeLa Kyoto cell lines stably expressing tubulin-GFP were seeded 24 h before at a plating density of 100,000 cells/cm^2 either directly on 24-well imaging slides (Ibidi) or on coverslips. For optimal adherence and monolayer growth, mESC-designated wells and coverslips were coated with 5 μg/ml laminin 511 in 1× PBS (supplemented with Ca^{2+} and Mg^{2+}). Media were taken off and replaced with microtubule-optimized fixation buffer containing 3.2% paraformaldehyde (EM Sciences) and 0.1% glutaraldehyde (EM Sciences) in 1× BRB80 (80 mM Pipes, 1 mM MgCl$_2$, and 1 mM EGTA, pH 6.8 with KOH) prewarmed to 37°C and incubated for 10 min at 37°C. Cells were washed three times in 1× PBS before quenching with 0.1 M glycine (Roth) in 1× PBS for 10 min at RT and 0.1% NaBH$_4$ (Sigma) in 1× PBS for 7 min at RT. DNA was stained with SiR-DNA at a final concentration of 250 nM. Cells were imaged directly in 1× PBS ("fixed only") or embedded in mounting media (ProLong anti-fade; Invitrogen) and mounted on cover slides (“fixed + mounted”).

For benchmarking of the Spindle3D analysis (see Image analysis reliability and accuracy; Fig. S4 A), spindle poles were immunostained using anti-γ-tubulin antibodies (T6557; Sigma). Cells grown on 24-well imaging slides (Ibidi) were fixed as described above. After quenching, cells were immersed in blocking buffer (3% BSA and 0.1% Triton X-100 in 1× PBS) for 1 h at RT. Primary antibodies were diluted 1:100 in blocking buffer. Incubation with primary antibodies was performed for 1 h at RT under gentle agitation. After three 1x PBS washes for 5 min each, cells were treated with 2 µg/ml anti-mouse Alexa Fluor 568–labeled secondary antibodies (A-11061; Thermo Fisher Scientific) in blocking buffer for 45 min at RT and constant agitation. After three final washes with 1× PBS (5 min each), DNA was stained with Hoechst 33343 (62249; Thermo Fisher Scientific) at a final concentration of 2 µM and imaged in 1× PBS.

Image acquisition

For imaging, HeLa Kyoto, Ptk$_2$, and HEK293 cells were incubated in imaging medium containing FluoroBrite DMEM (Gibco) supplemented with 10% FBS (Gibco), 4 mM L-glutamine (Invitrogen), and antibiotic–antimycotic (Invitrogen). mESCs were incubated in stem cell imaging medium containing FluoroBrite DMEM (Gibco) supplemented with 16% FBS (Gibco), nonessential amino acids (Gibco), β-mercaptoethanol (Gibco), sodium pyruvate (Gibco), antibiotic–antimycotic (Invitrogen), and mouse leukemia inhibitory factor (ESGRO). To visualize chromosomes, cells were treated with a final concentration of 250 nM SiR-DNA (Spirochrome). Since Ptk$_2$ cells did not show any incorporation of SiR-DNA, we instead incubated the cells for 5 min with Hoechst 33343 (62249; Thermo Fisher Scientific) at a final concentration of 2 µM in 1× PBS and replaced the staining solution with imaging medium. Live-cell imaging was performed using stabilized incubation systems at 37°C and 5% CO$_2$.

Imaging was performed on multiple setups

R1/E mESCs were imaged on a Zeiss LSM 800 system (sampling in xy, 0.27 µm; z step size, 0.75 µm; total number of slices, 32; pinhole, 48.9 µm; unidirectional scan speed, 10; averaging, 2) using a C-Apochromat 40× water objective (1.2 NA), 488-nm (0.1% power) and 640-nm (0.1% power) laser lines, and detection ranges of 410–558 nm and 586–700 nm, respectively. Images were acquired using ZEN 2.6 (blue edition; Zeiss). During imaging, cells were incubated using a custom-built incubation chamber (European Molecular Biology Laboratories workshop).

HEK293 cells were imaged on a Nikon spinning disk (CSU-X) confocal system equipped with an electron-multiplying charge-coupled device camera (iXon3 DU-888 Ultra, 1,024 × 1,024 pixels, and 13-µm pixel size) using a 60× plan apochromat (Plan-Apo) oil (1.4 NA) objective (sampling in xy, 0.22 µm. z step size, 0.3 µm. total number of slices, 150), 405-nm (9% power) and 640-nm (10% power) laser lines, and an excitation time of 200 ms. The microscope was operated using NIS Elements software (Nikon).

Ptk$_2$ cells were imaged on the same system using a 40× Plan-Fluor 40X 1.3 NA oil objective (1.3 NA) objective (sampling in xy, 0.34 µm; z step size, 0.3 µm; total number of slices, 100–150) and 405-nm (10% power, 100 ms excitation) and 488-nm (18% power, 300 ms excitation) laser lines.

HeLa Kyoto cells were imaged on the same system using a 60× Plan-Apo oil (1.4 NA) objective (see above) or a 100× Plan-Apo oil (1.45 NA) objective (sampling in xy, 0.14 µm; z step size, 0.2 µm; z ranges were selected individually per region of interest) using 488-nm (20% power, 100 ms excitation) and 640-nm (12% power, 100 ms excitation) laser lines. Fixed samples of mESCs and HeLa Kyoto cells were recorded on a Nikon spinning disk (CSU-X) confocal system (see above) using a 60× Plan-Apo oil (1.4 NA) objective (see above).

Bovine embryos were generated as previously described (Cavazza et al., 2021). Before fertilization, bovine eggs were injected with 4 pl mRNAs for mClover3-MAP4-MTBD at 200 ng/µl and for H2B-mScarlet at 60 ng/µl. Bovine embryos were imaged in 20 µl BO-IVC (IVF Biosciences) at 38.8°C, 5% CO$_2$, 6% O$_2$ under paraffin oil in a 35-mm dish with a #1.0 coverslip. Images were acquired with LSM 800 confocal laser scanning microscopes (Zeiss) equipped with an environmental incubator box and a 40× C-apochromat (1.2 NA) water-immersion objective. The system was operated using ZEN 2.3 (blue edition; Zeiss). A volume of 65 µm × 65 µm × 60 µm centered on the chromosomes was typically recorded. The optical slice thickness was 3.00 µm at a z step size of 2.5 µm. Each embryo was typically imaged every 5 or 10 min using the lowest possible laser intensity (>0.2% for the 488-nm laser and >0.2% for the 561-nm laser). mClover3 was excited with a 488-nm laser line and detected at 493–571 nm. mScarlet was excited with a 561-nm laser line and detected at 571–638 nm.

Image processing and analysis

After imaging, the only preprocessing step required for downstream analysis is a manual crop of the mitotic cells of interest from the raw files. We suggest using the rectangular selection tool in Fiji (Schindelin et al., 2012). Please note that the morphometric analysis only works on spindles and chromatin that were fully captured in z. Furthermore, the analysis requires fluorescent information of spindle microtubules and chromatin in separate channels that are specified by the user. Other channels will be ignored but displayed in the output image. A set of reference input images is provided with the plug-in.

Our automated analysis of chromosomes and spindles is in many aspects similar to the MATLAB-based algorithms described in Schneider et al. (2021). To make such methodology available to a wider user base, we implemented our image processing in ImgLib2 (Pietzsch et al., 2012) and distributed Spindle3D (https://github.com/tischi/spindle3d) as a Fiji plug-in that can be installed by enabling the Spindle3D update site (https://sites.imagej.net/Spindle3D). The image processing and analysis pipeline runs fully automated and consists of the below steps. Parameters are shown in quotation marks, with the default parameter values indicated after a colon.

Isotropic resampling

To facilitate implementation of the image analysis algorithms all channels of the input image are resampled to an isotropic voxel size (“voxel size for analysis”: 0.25 µm).

For metaphase plate initial segmentation, to find the location of the metaphase plate in the image, we rely on the fact that the DNA signal in condensed chromosomes is brighter than interphase DNA. To find an intensity threshold above which voxels belong to condensed (metaphase) chromosomes, we first downsample the DNA image such that the width of one voxel resembles the typical width of the metaphase plate (“voxel size for initial DNA threshold” 1.5 µm; see Fig. S1 A, left). The intensity values in the downsampled image are computed by averaging with a gaussian blur with a sigma of half the voxel size for initial DNA threshold. In this downsampled image, we find the maximal and minimal intensity. We empirically determined that (maximal + minimal)/2 serves as a reliable threshold. We then apply this threshold to the DNA image to create a binary mask and perform a connected component labeling (Fig. S1 A, center). We remove all connected components that touch the lateral (xy) image boundary and of the remaining ones only keep the largest one, which we define to be the initial metaphase plate object.

Metaphase plate center and orientation

To determine the orientation of the metaphase plate, we use an algorithm from ImageJ’s 3D Suite (Ollion et al., 2013) to fit a 3D ellipsoid to the initial metaphase plate object, resulting in three vectors along the shortest, middle, and longest axes as well as the coordinates of the metaphase plate center. To facilitate the implementation of the subsequent algorithms (e.g., in terms of specifying ranges to be included in certain computations) and facilitate visual inspection of the images, we use these vectors to compute a transformation that puts all images into a new coordinate system such that the new z axis corresponds to the shortest axis of the metaphase plate, roughly corresponding to the spindle pole-to-pole axis, and such that the origin of the coordinate system coincides with the center of the metaphase plate. We will refer to these transformed images as metaphase plate aligned images (Fig. S1 A, right).

Metaphase plate width

Using the metaphase plate–aligned DNA image, we compute an average intensity profile along the shortest DNA axis (z axis of the aligned image), limiting the computations to a maximum width that is based on the extent of the shortest axis of the initial ellipsoid fit times 2. We then compute the derivative of this profile at a resolution of “metaphase plate derivative delta” 3 µm. We define the metaphase plate width as the distance between the locations with the highest absolute values in the derivative (see Fig. S1 B, left). This procedure is motivated by the fact that, due to the various chromosomes and the diffraction limit of the microscope, the metaphase plate has an overall irregular appearance. For example, our analysis is robust to an individual chromosome “sticking out” of the metaphase plate as this will not shift above maxima of the derivatives (see Fig. S1 B, left). In other words, our approach measures an average width, determined by the average position of all chromosomes.

Metaphase plate length

Using the metaphase plate–aligned DNA image, we compute an average lateral radial intensity profile (see Fig. S1 B, center left), limiting the computations to a maximum length determined by the extent of the longest axis in the initial ellipsoid fit times 2. We define the metaphase plate length as two times the distance between the origin to the position of the minimum in the derivative of the intensity profile. Again, this approach reports an average measurement that is robust to any details that the various arrangements of the chromosomes in the metaphase plate may have. In addition, both the measurements of the metaphase width and length have the advantage of not depending on the choice of any intensity threshold.

Chromatin dilation

We further use the average lateral radial DNA intensity profile (see above) to calculate the ratio of the intensity in the center of the metaphase plate (position zero along the radial profile) and the brightest part along the profile (see Fig. S1 B, center right). This ratio is subtracted from 1 to report on the magnitude of the dilation in the center of the metaphase plate, with higher values corresponding to a more pronounced opening and smaller values reflecting homogeneously closed metaphase plates.

Chromatin volume

To facilitate the comparison with previously published measurements, we decided to adopt the method of Hériché et al., (2014), where the Otsu algorithm (Otsu, 1979) is used to determine an intensity threshold and the chromatin volume is determined as the sum of the volume of all voxels above this threshold. The Otsu algorithm relies on a bimodal (foreground and background) intensity distribution. We therefore apply the Otsu algorithm to a region of interest determined by the previously measured metaphase plate width and length (see Fig. S1 B, right), where the intensity values comprise only the metaphase plate (foreground) and parts of the cell devoid of DNA signal (background) and exclude (unwanted) DNA signals from surrounding cells. We apply the determined threshold to the whole image, perform a connected component analysis, remove regions touching the image borders, and keep the largest region, which we call segmented metaphase plate. The volume of this region is the chromatin volume.

Spindle segmentation

We explored various methods of reliably determining an intensity threshold for assigning pixels to the mitotic spindle and developed an algorithm relying on the observation that, in all data we analyzed, the metaphase plate length was always substantially (on average 25%) larger than the spindle width. The direct vicinity of the metaphase plate therefore contains a substantial fraction of pixels inside and outside the spindle. Thus, this region is well suited for determining an automated threshold using the Otsu algorithm (see Chromatin volume). Technically, we apply the Otsu algorithm to all tubulin intensity values in a rim of a thickness of 1 pixel around the segmented metaphase plate (see Fig. S1 C, center left). We then apply this threshold to the whole tubulin image and perform a connected component analysis. As there can be other cells with relatively bright tubulin intensities in the same image, we filter the regions, only keeping regions where at least one of their pixels is within a defined distance to the center of the metaphase plate ("spindle fragment inclusion zone" 3 µm). We will refer to the union of those regions as the spindle mask.

Spindle volume

The spindle volume is computed as the volume of all voxels in the spindle mask (see Fig. S1 C, center left).

Spindle average intensity

The spindle average intensity is the average gray value of all tubulin voxels within the spindle volume mask.

Spindle intensity variation

Spindles have different degrees of homogeneity in terms of their distribution of polymerized tubulin. We measure this by computing the coefficient of variation of the (threshold subtracted) tubulin intensities within the spindle mask.

Spindle poles locations

In our algorithm, both spindle length and spindle orientation are determined by the vector that connects the two spindle poles. We locate the spindle poles in two steps. First, we draw a line profile through the spindle mask along the shortest metaphase plate axis and through the metaphase plate center. The two locations along the line profile where the spindle mask intensity drops from 1 to 0 (i.e., the spindle mask ends) are the two initial spindle poles (see Fig. S1 C, center right). As the spindle axis is often not completely aligned with the shortest metaphase plate axis, the initial spindle poles need to be refined. To do so, we determine the locations of the pixels with the maximum intensity in the tubulin image in a small neighborhood around the initial spindle poles. The extent of this neighborhood is controlled by the "axial pole refinement radius" (1.0 µm) and the "lateral pole refinement radius" (2.0 µm), where axial refers to along the shortest metaphase plate axis and lateral refers to the perpendicular directions (see Fig. S1 C, center right).

Spindle center location

We define the middle between the two spindle poles as the spindle center location.

Spindle center to metaphase plate center distance

The spindle center to metaphase plate center distance is the distance of the metaphase plate center (see above) to the spindle center.

Spindle length

We define the spindle length as the distance between the two spindle poles (see Fig. S1 C, center right).

Spindle angle

The two spindle poles allow us to define a spindle axis vector that points from one pole to the other. We apply the following formula (in the coordinate system of the input data, where we assume the coverslip plane to be perpendicular to the z axis) to compute the angle of the spindle axis and the coverslip plane: 90.0 − absolute(angle_degrees(z_axis, spindle-axis)). For the computation of an angle between two axes there are always two solutions. Here, the computations within the function angle_degrees are done such that the smaller one, i.e., with a value between 0 and 90 degrees, is picked (see Fig. S1 C, right).

Spindle coordinate system

We define a new coordinate system in which the spindle center is at the origin and the spindle poles are aligned along the z axis. This coordinate system simplifies the following measurement.

Spindle widths

To measure the spindle width we perform a maximum projection of the spindle mask along the spindle axis (the z axis in the spindle coordinate system). We smoothen the 2D projected spindle mask by a morphological opening operation with a radius of 2 pixels. We then compute the width of the binary mask in steps of 10 degrees (see Fig. S1 C, center right). We define the mean of the resulting widths as the average spindle width. To capture potential anisotropies in the spindle shape, we fetch both the minimum and maximum of the width at all measured angles, resulting in the outputs "minimal spindle width" and "maximal spindle width."

Spindle aspect ratio

As a measure for spindle shape, we define the ratio of spindle length and the average spindle width as the spindle aspect ratio.

Tabular output

The plug-in outputs all measured values in a table, where the column names correspond to the respective measurements.

Image output

The plug-in also outputs a multichannel image, composed of the DNA and tubulin signal, the DNA mask, the spindle mask, and another image containing three points corresponding to the spindle poles and the spindle center (see Fig. 2 B). All images are sampled isotropically at the voxel size for analysis. For ease of inspection, all images are aligned such that the x axis corresponds to the measured spindle axis and the center of the image corresponds to the spindle center.

Cell volume quantification

Cells expressing tubulin genetically fused to a fluorescent protein show characteristic cytoplasmic background fluorescence (see Fig. 5 A). We used the machine learning–based segmentation software Ilastik (Berg et al., 2019) to train pixel-classification models to distinguish between true mitotic cytoplasm and all other voxels. Before training and prediction, all images were rescaled to an isotropic voxel size of 0.25 µm to be consistent with the analysis voxel size applied in the Spindle3D analyses. For training, training set images were annotated in the autocontext module in Ilastik, a two-step workflow, where the second stage receives the prediction results from the initial stage. In the first stage, the default random forest algorithm was trained with the classes "spindle microtubules," "mitotic cytoplasm," "interphase microtubules," and "background." Brightness features were excluded to avoid bias in fluorescence signal strength (i.e., varying expression levels of fluorescent tubulin). We used all available texture and edge filters for training. In the second stage, we trained another random forest to distinguish between the two classes “true mitotic” and “other,” while again all brightness features were ignored and all texture and edge features were included. After successful training, batch processing was performed using the Ilastik integration in Fiji. The second-stage probability masks (see Fig. 5 A, center) were denoised with a 3D Gaussian filter (sigma = 2 pixels) and thresholded at the cutoff value 0.5, reflecting the binary prediction approach to distinguish between true mitotic and other. The resulting segmentation masks (see Fig. 5 A, right) were provided alongside the raw voxel images for analysis in Spindle3D, where cell volumes and cell surface areas were quantified using the 3D ImageJ Suite’s (Ollion et al., 2013) volume and corrected area algorithms, respectively.

Spindle mass quantification

In cells expressing fluorescently tagged tubulin, we can define the average voxel gray value within the cell mask (see Cell volume quantification) as the average concentration of tubulin in the whole cell, $[\mathrm{Tub}]_C$. Analogously, the average concentration of tubulin in the spindle, $[\mathrm{Tub}]_S$, is reflected by the average voxel value within the spindle mask. To account for system-internal noise of the imaging setup, we calculated the median voxel values in the bottommost slices of the image stack. We then subtracted this value from both $[\mathrm{Tub}]_C$ and $[\mathrm{Tub}]_S$.

We define spindle mass as the sum of tubulin (free and polymer) within the spindle volume V_S. To correct for cell-specific tubulin-GFP expression levels, we normalized spindle masses by the cell-specific fluorescence correction factor $Fl_{corr} \sim [\mathrm{Tub}]_C$: spindle mass $m_s = [\mathrm{Tub}]_S \times V_S/Fl_{corr}$. We derive the normalized tubulin density (free and polymer) within the spindle via $\rho_S = m_s/V_S$.

Image analysis reliability and accuracy

To benchmark the measurements of the plug-in, we labeled centrosomes of tubulin-GFP–expressing R1/E mESCs with anti-γ-tubulin antibodies (see Chemical fixation and immunostaining of tissue culture cells). Having imaged the spindles using confocal microscopy, we located the outward-facing edges of the γ-tubulin signals and defined their 3D coordinates as the ground-truth spindle poles (see Fig. S3 A) in Fiji. The Euclidean distance between the two poles was defined as the ground-truth spindle length. In parallel, we located the 3D coordinates of the poles exclusively by looking at the tubulin-GFP signals. The Euclidean distance between this pair of poles was defined as the manual spindle length. Ultimately, we compared both the ground-truth spindle length and the manual spindle length measurements to measurements derived via the Spindle3D plug-in.

Opposed to spindle length, we lack proper ground-truth references for spindle width. Nevertheless, we benchmarked the plug-in’s performance against human measurement. To this end, we made use of the spindle axis registration of the Spindle3D analysis and verified the orientation with the centrosomal γ-tubulin signals (see above). In Fiji, we used Image > Stack > Reslice to match the direction of the spindle axis with the z axis and performed a maximum projection. Using only the tubulin-GFP and γ-tubulin signals, we manually determined four extents of the spindle in the projected image (see Fig. S3 B) and calculated their mean to serve as the manual spindle width reference measurement.

To verify the performance of the pixel classification–based mitotic cell volume quantification, we transfected tubulin-GFP–expressing HeLa Kyoto cells with plasmids encoding mCherry tagged with the CaaX motif (Clarke, 1992) for cell membrane localization. We acquired confocal images of mCherry-positive mitotic cells (see Fig. S4 A) and performed our tubulin-GFP based cell volume quantification as described above. In parallel, we manually segmented cell volumes using the mCherry-CaaX landmark channel and the volume manager in the SCF MPI-CBG Fiji package (https://sites.imagej.net/SCF-MPI-CBG/; see Fig. S4 B) to generate a binary cell mask, the volume of which was quantified via the “3D analyse regions” function in the MorphoLibJ package (Legland et al., 2016).

For quality control, 3D image stacks were rendered using the multichannel visualization package ClearVolume (Royer et al., 2015) in Fiji.

Data analysis and visualization

After image analysis, we used the pandas (The Pandas Development Team, 2020), SciPy (Virtanen et al., 2020), and NumPy (Harris et al., 2020) libraries in Python to further analyze the data. Spearman correlation coefficients were calculated in the SciPy stats.spearman package. The P values given indicate the probability of an uncorrelated system producing datasets that have a Spearman correlation at least as extreme. Statistical tests (Wilcoxon signed-rank test) were performed using the scipy.stats package. ANOVA and post-hoc testing were performed using the Python statsmodel package (Seabold and Perktold, 2010). Linear regression was performed in the scikit-learn package (Pedregosa et al., 2011). All data visualization was performed in the Python Altair library (VanderPlas et al., 2018) and assembled in Adobe Illustrator 2021.

Online supplemental material

Fig. S1 shows the Spindle3D image analysis workflow. Fig. S2 shows the relationship between genome sizes and spindle and chromatin dimensions. Fig. S3 compares the analytical performance of Spindle3D with manual morphometric measurements. Fig. S4 shows additional reference cell volume quantifications. Fig. S5 shows that cell surface area to volume ratios do not explain the unique spindle scaling phenotype of Ptk_2 cells.

Data availability

Raw imaging data used for the study have been deposited in BioStudies under the accession number S-BSST669. Spindle3D (https://github.com/tischi/spindle3d) is distributed as a Fiji plug-in and can be installed by enabling the Spindle3D update site (https://sites.imagej.net/Spindle3D).

Acknowledgments

We thank all present and past members of the Reber laboratory and the Advanced Light Microscopy Facility at the European

Molecular Biology Laboratory for support, in particular Aliaksandr Halavatyi and Faba Neumann. We thank the Advanced Medical BIOimaging Core Facility (AMBIO) at the Charité Berlin for imaging support. We thank Jean-Karim Hériché and Julius Hossain (both European Molecular Biology Laboratory) for advice on image analysis. We are grateful to Renata Basto and Melina Schuh and their laboratories for testing the plug-in and for critical discussions. We thank Christopher Schmied, Stefan Terjung, and Jan Brugues for critical comments on the manuscript.

This work was supported by the Deutsche Forschungsgemeinschaft (A Quantitative Force Map of the Mitotic Spindle, RE 3925/1-1 to S. Reber) and the Horizon 2020 Framework Programme of the European Union (iNEXT grant 653706, project PID 3503 to S. Reber). S. Reber further acknowledges funding by IRI Life Sciences (Humboldt-Universität zu Berlin, Excellence Initiative/ Deutsche Forschungsgemeinschaft).

The authors declare no competing financial interests.

Author contributions: S. Reber contributed to conceptualization and funding acquisition. T. Kletter carried out all experiments. S. Reusch and N. Dempewolf acquired selected datasets and performed quality control analyses. T. Cavazza acquired bovine data sets. T. Kletter and C. Tischer constructed the plug-in, analyzed images, and performed data analysis. S. Reber wrote the paper, with input from all authors.

Submitted: 28 June 2021
Revised: 20 October 2021
Accepted: 21 October 2021

References

Baran, V., A. Brzakova, P. Rehak, V. Kovarikova, and P. Solc. 2016. PLK1 regulates spindle formation kinetics and APC/C activation in mouse zygote. *Zygote.* 24:338–345. https://doi.org/10.1017/S0967199415000246

Berg, S., D. Kutra, T. Kroeger, C.N. Straehle, B.X. Kausler, C. Haubold, M. Schiegg, J. Ales, T. Beier, M. Rudy, et al. 2019. ilastik: interactive machine learning for (bio)image analysis. *Nat. Methods.* 16:1226–1232. https://doi.org/10.1038/s41592-019-0582-9

Bird, A.W., and A.A. Hyman. 2008. Building a spindle of the correct length in human cells requires the interaction between TPX2 and Aurora A. *J. Cell Biol.* 182:289–300. https://doi.org/10.1083/jcb.200802005

Brown, K.S., M.D. Blower, T.J. Maresca, T.C. Grammer, R.M. Harland, and R. Heald. 2007. Xenopus tropicalis egg extracts provide insight into scaling of the mitotic spindle. *J. Cell Biol.* 176:765–770. https://doi.org/10.1083/jcb.200610043

Brownlee, C., and R. Heald. 2019. Importin α Partitioning to the Plasma Membrane Regulates Intracellular Scaling. *Cell.* 176:805–815.e8. https://doi.org/10.1016/j.cell.2018.12.001

Bylund, L., S. Kytölä, W.O. Lui, C. Larsson, and G. Weber. 2004. Analysis of the cytogenetic stability of the human embryonal kidney cell line 293 by cytogenetic and STR profiling approaches. *Cytogenet. Genome Res.* 106: 28–32. https://doi.org/10.1159/000078556

Cai, Y., M.J. Hossain, J.K. Hériché, A.Z. Politi, N. Walther, B. Koch, M. Wachsmuth, B. Nijmeijer, M. Kueblbeck, M. Martinic-Kavur, et al. 2018. Experimental and computational framework for a dynamic protein atlas of human cell division. *Nature.* 561:411–415. https://doi.org/10.1038/s41586-018-0518-z

Cavazza, T., P. Malgaretti, and I. Vernos. 2016. The sequential activation of the mitotic microtubule assembly pathways favors bipolar spindle formation. *Mol. Biol. Cell.* 27:2935–2945. https://doi.org/10.1091/mbc.E16-05-0322

Cavazza, T., Y. Takeda, A.Z. Politi, M. Aushev, P. Aldag, C. Baker, M. Choudhary, J. Bucevičius, G. Lukinavičius, K. Elder, et al. 2021. Parental genome unification is highly error-prone in mammalian embryos. *Cell.* 184:2860–2877.e22. https://doi.org/10.1016/j.cell.2021.04.013

Clarke, S. 1992. Protein isoprenylation and methylation at carboxyl-terminal cysteine residues. *Annu. Rev. Biochem.* 61:355–386. https://doi.org/10.1146/annurev.bi.61.070192.002035

Courtois, A., M. Schuh, J. Ellenberg, and T. Hiiragi. 2012. The transition from meiotic to mitotic spindle assembly is gradual during early mammalian development. *J. Cell Biol.* 198:357–370. https://doi.org/10.1083/jcb.201202135

Crowder, M.E., M. Strzelecka, J.D. Wilbur, M.C. Good, G. von Dassow, and R. Heald. 2015. A comparative analysis of spindle morphometrics across metazoans. *Curr. Biol.* 25:1542–1550. https://doi.org/10.1016/j.cub.2015.04.036

Decker, F., D. Oriola, B. Dalton, and J. Brugués. 2018. Autocatalytic microtubule nucleation determines the size and mass of *Xenopus laevis* egg extract spindles. *eLife.* 7:e31149. https://doi.org/10.7554/eLife.31149

Dinarina, A., C. Pugieux, M.M. Corral, M. Loose, J. Spatz, E. Karsenti, and F. Nédélec. 2009. Chromatin shapes the mitotic spindle. *Cell.* 138:502–513. https://doi.org/10.1016/j.cell.2009.05.027

Dumont, S., and T.J. Mitchison. 2009. Compression regulates mitotic spindle length by a mechanochemical switch at the poles. *Curr. Biol.* 19: 1086–1095. https://doi.org/10.1016/j.cub.2009.05.056

Farhadifar, R., C.F. Baer, A.C. Valfort, E.C. Andersen, T. Müller-Reichert, M. Delattre, and D.J. Needleman. 2015. Scaling, selection, and evolutionary dynamics of the mitotic spindle. *Curr. Biol.* 25:732–740. https://doi.org/10.1016/j.cub.2014.12.060

Good, M.C., M.D. Vahey, A. Skandarajah, D.A. Fletcher, and R. Heald. 2013. Cytoplasmic volume modulates spindle size during embryogenesis. *Science.* 342:856–860. https://doi.org/10.1126/science.1243147

Goshima, G., and J.M. Scholey. 2010. Control of mitotic spindle length. *Annu. Rev. Cell Dev. Biol.* 26:21–57. https://doi.org/10.1146/annurev-cellbio-100109-104006

Grenfell, A.W., M. Strzelecka, M.E. Crowder, K.J. Helmke, A.L. Schlaitz, and R. Heald. 2016. A versatile multivariate image analysis pipeline reveals features of Xenopus extract spindles. *J. Cell Biol.* 213:127–136. https://doi.org/10.1083/jcb.201509079

Gruss, O.J., R.E. Carazo-Salas, C.A. Schatz, G. Guarguaglini, J. Kast, M. Wilm, N. Le Bot, I. Vernos, E. Karsenti, and I.W. Mattaj. 2001. Ran induces spindle assembly by reversing the inhibitory effect of importin alpha on TPX2 activity. *Cell.* 104:83–93. https://doi.org/10.1016/S0092-8674(01)00193-3

Hara, Y., and A. Kimura. 2009. Cell-size-dependent spindle elongation in the Caenorhabditis elegans early embryo. *Curr. Biol.* 19:1549–1554. https://doi.org/10.1016/j.cub.2009.07.050

Hara, Y., and A. Kimura. 2013. An allometric relationship between mitotic spindle width, spindle length, and ploidy in Caenorhabditis elegans embryos. *Mol. Biol. Cell.* 24:1411–1419. https://doi.org/10.1091/mbc.e12-07-0528

Hara, Y., M. Iwabuchi, K. Ohsumi, and A. Kimura. 2013. Intranuclear DNA density affects chromosome condensation in metazoans. *Mol. Biol. Cell.* 24:2442–2453. https://doi.org/10.1091/mbc.e13-01-0043

Harris, C.R., K.J. Millman, S.J. van der Walt, R. Gommers, P. Virtanen, D. Cournapeau, E. Wieser, J. Taylor, S. Berg, N.J. Smith, et al. 2020. Array programming with NumPy. *Nature.* 585:357–362. https://doi.org/10.1038/s41586-020-2649-2

Hazel, J., K. Krutkramelis, P. Mooney, M. Tomschik, K. Gerow, J. Oakey, and J.C. Gatlin. 2013. Changes in cytoplasmic volume are sufficient to drive spindle scaling. *Science.* 342:853–856. https://doi.org/10.1126/science.1243110

Heald, R., and R. Gibeaux. 2018. Subcellular scaling: does size matter for cell division? *Curr. Opin. Cell Biol.* 52:88–95. https://doi.org/10.1016/j.ceb.2018.02.009

Heald, R., R. Tournebize, T. Blank, P. Becker, A. Hyman, and E. Karsenti. 1996. Self-organization of microtubules into bipolar spindles around artificial chromosomes in Xenopus egg extracts. *Nature.* 382(6590):420–425. https://doi.org/doi.org/10.1038/382420a0

Hériché, J.K., J.G. Lees, I. Morilla, T. Walter, B. Petrova, M.J. Roberti, M.J. Hossain, P. Adler, J.M. Fernández, M. Krallinger, et al. 2014. Integration of biological data by kernels on graph nodes allows prediction of new genes involved in mitotic chromosome condensation. *Mol. Biol. Cell.* 25: 2522–2536. https://doi.org/10.1091/mbc.e13-04-0221

Hirst, W.G., A. Biswas, K.K. Mahalingan, and S. Reber. 2020. Differences in Intrinsic Tubulin Dynamic Properties Contribute to Spindle Length Control in Xenopus Species. *Curr. Biol.* 30:2184–2190.e5. https://doi.org/10.1016/j.cub.2020.03.067

Kieserman, E.K., and R. Heald. 2011. Mitotic chromosome size scaling in Xenopus. *Cell Cycle*. 10:3863–3870. https://doi.org/10.4161/cc.10.22.17975

Lacroix, B., G. Letort, L. Pitayu, J. Sallé, M. Stefanutti, G. Maton, A.M. Ladouceur, J.C. Canman, P.S. Maddox, A.S. Maddox, et al. 2018. Microtubule Dynamics Scale with Cell Size to Set Spindle Length and Assembly Timing. *Dev. Cell*. 45:496–511.e6. https://doi.org/10.1016/j.devcel.2018.04.022

Ladouceur, A.M., J.F. Dorn, and P.S. Maddox. 2015. Mitotic chromosome length scales in response to both cell and nuclear size. *J. Cell Biol.* 209:645–651. https://doi.org/10.1083/jcb.201502092

Legland, D., I. Arganda-Carreras, and P. Andrey. 2016. MorphoLibJ: integrated library and plugins for mathematical morphology with ImageJ. *Bioinformatics*. 32:3532–3534. https://doi.org/10.1093/bioinformatics/btw413

Levy, D.L., and R. Heald. 2012. Mechanisms of intracellular scaling. *Annu. Rev. Cell Dev. Biol.* 28:113–135. https://doi.org/10.1146/annurev-cellbio-092910-154158

Lipp, J.J., T. Hirota, I. Poser, and J.M. Peters. 2007. Aurora B controls the association of condensin I but not condensin II with mitotic chromosomes. *J. Cell Sci.* 120:1245–1255. https://doi.org/10.1242/jcs.03425

Macville, M., E. Schröck, H. Padilla-Nash, C. Keck, B.M. Ghadimi, D. Zimonjic, N. Popescu, and T. Ried. 1999. Comprehensive and definitive molecular cytogenetic characterization of HeLa cells by spectral karyotyping. *Cancer Res.* 59:141–150.

Marshall, W.F. 2020. Scaling of Subcellular Structures. *Annu. Rev. Cell Dev. Biol.* 36:219–236. https://doi.org/10.1146/annurev-cellbio-020520-113246

McNally, F.J. 2013. Mechanisms of spindle positioning. *J. Cell Biol.* 200:131–140. https://doi.org/10.1083/jcb.201210007

Mora-Bermúdez, F., D. Gerlich, and J. Ellenberg. 2007. Maximal chromosome compaction occurs by axial shortening in anaphase and depends on Aurora kinase. *Nat. Cell Biol.* 9:822–831. https://doi.org/10.1038/ncb1606

Müller, P.M., et al. 2020. Systems analysis of RhoGEF and RhoGAP regulatory proteins reveals spatially organized RAC1 signalling from integrin adhesions. *Nature cell biology*. 22(4):498–511. https://doi.org/doi.org/10.1038/s41556-020-0488-x

Oh, D., C.H. Yu, and D.J. Needleman. 2016. Spatial organization of the Ran pathway by microtubules in mitosis. *Proc. Natl. Acad. Sci. USA*. 113:8729–8734. https://doi.org/10.1073/pnas.1607498113

Ollion, J., J. Cochennec, F. Loll, C. Escudé, and T. Boudier. 2013. TANGO: a generic tool for high-throughput 3D image analysis for studying nuclear organization. *Bioinformatics*. 29:1840–1841. https://doi.org/10.1093/bioinformatics/btt276

Otsu, N. 1979. A Threshold Selection Method from Gray-Level Histograms. *IEEE Trans. Syst. Man Cybern.* 9:62–66. https://doi.org/10.1109/TSMC.1979.4310076

Pedregosa, F., V. Michel, O. Grisel, M. Blondel, P. Prettenhofer, R. Weiss, J. VanderPlas, D. Cournapeau, G. Varoquaux, A. Gramfort, et al. 2011. Scikit-learn: Machine Learning in Python. *J. Mach. Learn. Res.* 12:2825–2830.

Pietzsch, T., S. Preibisch, P. Tomancák, and S. Saalfeld. 2012. ImgLib2--generic image processing in Java. *Bioinformatics*. 28:3009–3011. https://doi.org/10.1093/bioinformatics/bts543

Reber, S., and N.W. Goehring. 2015. Intracellular scaling mechanisms. *Cold Spring Harb. Perspect. Biol.* 7:a019067. https://doi.org/10.1101/cshperspect.a019067

Reber, S., and A.A. Hyman. 2015. Emergent properties of the metaphase spindle. *Cold Spring Harb. Perspect. Biol.* 7:a015784. https://doi.org/10.1101/cshperspect.a015784

Reber, S.B., J. Baumgart, P.O. Widlund, A. Pozniakovsky, J. Howard, A.A. Hyman, and F. Jülicher. 2013. XMAP215 activity sets spindle length by controlling the total mass of spindle microtubules. *Nat. Cell Biol.* 15:1116–1122. https://doi.org/10.1038/ncb2834

Rens, W., P.C. O'Brien, F. Yang, J.A. Graves, and M.A. Ferguson-Smith. 1999. Karyotype relationships between four distantly related marsupials revealed by reciprocal chromosome painting. *Chromosome Res.* 7:461–474. https://doi.org/10.1023/a:1009249813617

Rieckhoff, E.M., F. Berndt, M. Elsner, S. Golfier, F. Decker, K. Ishihara, and J. Brugués. 2020. Spindle Scaling Is Governed by Cell Boundary Regulation of Microtubule Nucleation. *Curr. Biol.* 30:4973–4983.e10. https://doi.org/10.1016/j.cub.2020.10.093

Royer, L.A., M. Weigert, U. Günther, N. Maghelli, F. Jug, I.F. Sbalzarini, and E.W. Myers. 2015. ClearVolume: open-source live 3D visualization for light-sheet microscopy. *Nat. Methods*. 12:480–481. https://doi.org/10.1038/nmeth.3372

Schindelin, J., I. Arganda-Carreras, E. Frise, V. Kaynig, M. Longair, T. Pietzsch, S. Preibisch, C. Rueden, S. Saalfeld, B. Schmid, et al. 2012. Fiji: an open-source platform for biological-image analysis. *Nat. Methods*. 9:676–682. https://doi.org/10.1038/nmeth.2019

Schneider, I., M. de Ruijter-Villani, M.J. Hossain, T.A.E. Stout, and J. Ellenberg. 2021. Dual spindles assemble in bovine zygotes despite the presence of paternal centrosomes. *J. Cell Biol.* 220:e202010106. https://doi.org/10.1083/jcb.202010106

Seabold, S., and J. Perktold. 2010. Statsmodels: Econometric and statistical modeling with python. *Proceedings of the 9th Python in Science Conference*. 57:61. https://doi.org/10.25080/MAJORA-92BF1922-011

So, C., K.B. Seres, A.M. Steyer, E. Mönnich, D. Clift, A. Pejkovska, W. Möbius, and M. Schuh. 2019. A liquid-like spindle domain promotes acentrosomal spindle assembly in mammalian oocytes. *Science*. 364:eaat9557. https://doi.org/10.1126/science.aat9557

Takagi, J., T. Itabashi, K. Suzuki, T.M. Kapoor, Y. Shimamoto, and S. Ishiwata. 2013. Using micromanipulation to analyze control of vertebrate meiotic spindle size. *Cell Rep.* 5:44–50. https://doi.org/10.1016/j.celrep.2013.09.021

Takagi, J., T. Itabashi, K. Suzuki, Y. Shimamoto, T.M. Kapoor, and S. Ishiwata. 2014. Micromechanics of the vertebrate meiotic spindle examined by stretching along the pole-to-pole axis. *Biophys. J.* 106:735–740. https://doi.org/10.1016/j.bpj.2013.12.033

The Pandas Development Team 2020. pandas-dev/pandas: Pandas v1.1.3. *Zenodo*. https://doi.org/10.5281/zenodo.4067057

VanderPlas, J., B. Granger, J. Heer, D. Moritz, K. Wongsuphasawat, A. Satyanarayan, A. Lees, I. Timofeev, B. Welsh, and S. Sievert. 2018. Altair: Interactive Statistical Visualizations for Python. *J. Open Source Softw.* 3:1057. https://doi.org/10.21105/joss.01057

Virtanen, P., R. Gommers, T.E. Oliphant, M. Haberland, T. Reddy, D. Cournapeau, E. Burovski, P. Peterson, W. Weckesser, J. Bright, SciPy 1.0 Contributors, et al. 2020. SciPy 1.0: fundamental algorithms for scientific computing in Python. *Nat. Methods*. 17:261–272. https://doi.org/10.1038/s41592-019-0686-2

Wang, Z.W., G.L. Zhang, H. Schatten, J. Carroll, and Q.Y. Sun. 2016. Cytoplasmic Determination of Meiotic Spindle Size Revealed by a Unique Inter-Species Germinal Vesicle Transfer Model. *Sci. Rep.* 6:19827. https://doi.org/10.1038/srep19827

Wilbur, J.D., and R. Heald. 2013. Mitotic spindle scaling during Xenopus development by kif2a and importin α. *eLife*. 2:e00290. https://doi.org/10.7554/eLife.00290

Wühr, M., Y. Chen, S. Dumont, A.C. Groen, D.J. Needleman, A. Salic, and T.J. Mitchison. 2008. Evidence for an upper limit to mitotic spindle length. *Curr. Biol.* 18:1256–1261. https://doi.org/10.1016/j.cub.2008.07.092

Supplemental material

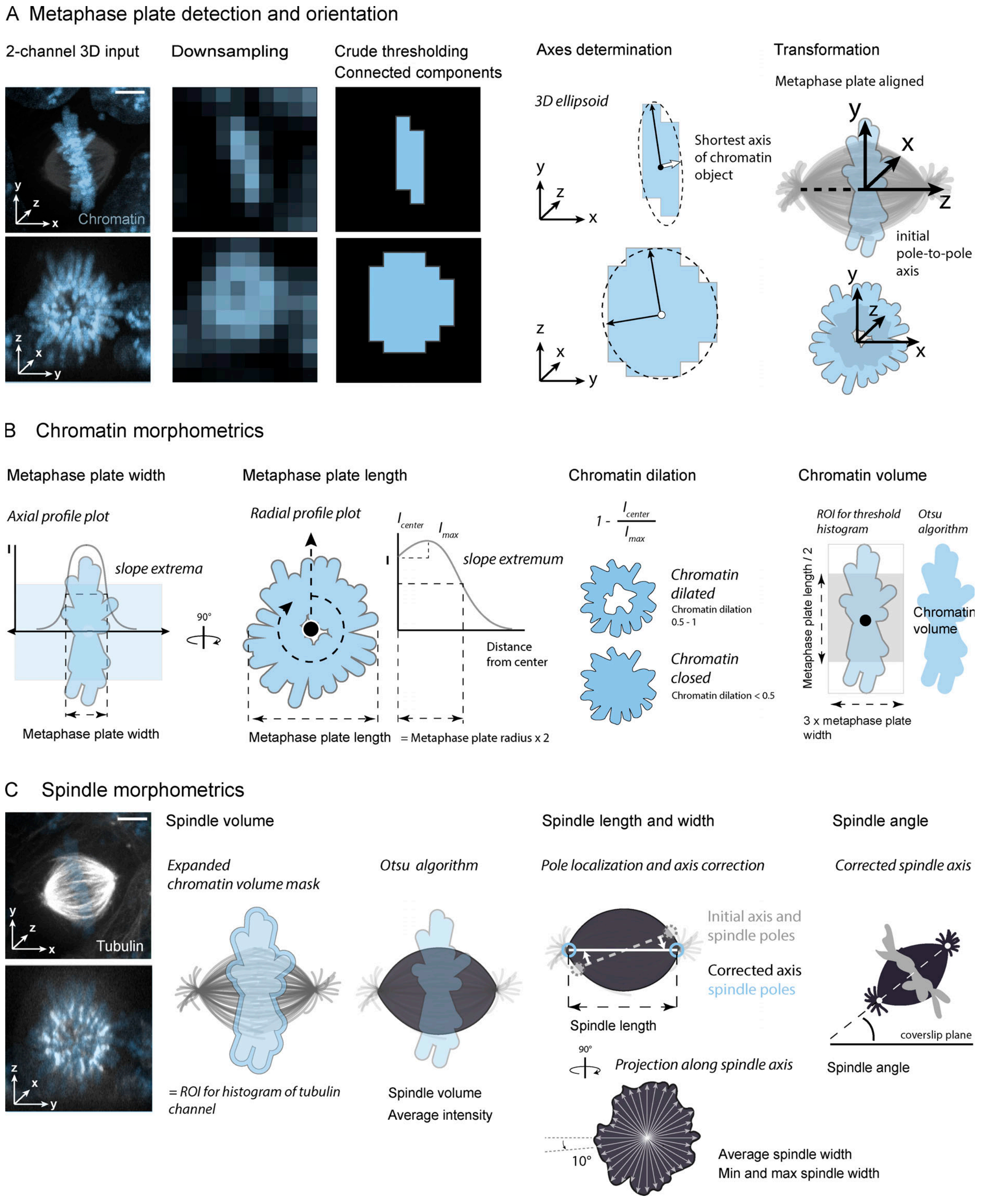

Figure S1. **Spindle3D morphometric analysis workflow. (A)** In confocal micrographs, mitotic cells (chromatin is shown in blue, and tubulin is shown in grayscale) are detected by crude, histogram-based segmentation and connected component analysis. The shortest axis of the metaphase plate object is determined and initiates an imaging axis-independent coordinate system. Scale bar, 5 µm. **(B)** In the newly aligned image, radial and axial intensity profiles serve as robust guides to quantify the extents of the usually irregularly shaped chromatin plate. Moreover, radial profiles inform on the magnitude of dilation of the metaphase plate. Based on the extents of the plate, a 3D region of interest is used to limit the pixels considered for histogram-based segmentation of the chromosomes, excluding potentially interfering signals from nuclei in close proximity. **(C)** Analogously, only a fraction of the tubulin channel pixels (the ones immediately bordering the chromatin mask and thus either represent spindle microtubules or nonspindle tubulin inside the cell) are considered for Otsu thresholding the spindle. Spindle poles are the brightest pixels found within defined radii around the intersections of the initial spindle axis (found in A) and the spindle volume mask. This mask is projected along the now corrected spindle axis. The resulting area is radially scanned in 10° steps to ultimately measure 18 lateral spindle extents, their mean representing the average spindle width. Finally, the tilt of the corrected spindle axis is used to determine the spindle angle. Scale bar, 5 µm. ROI, region of interest.

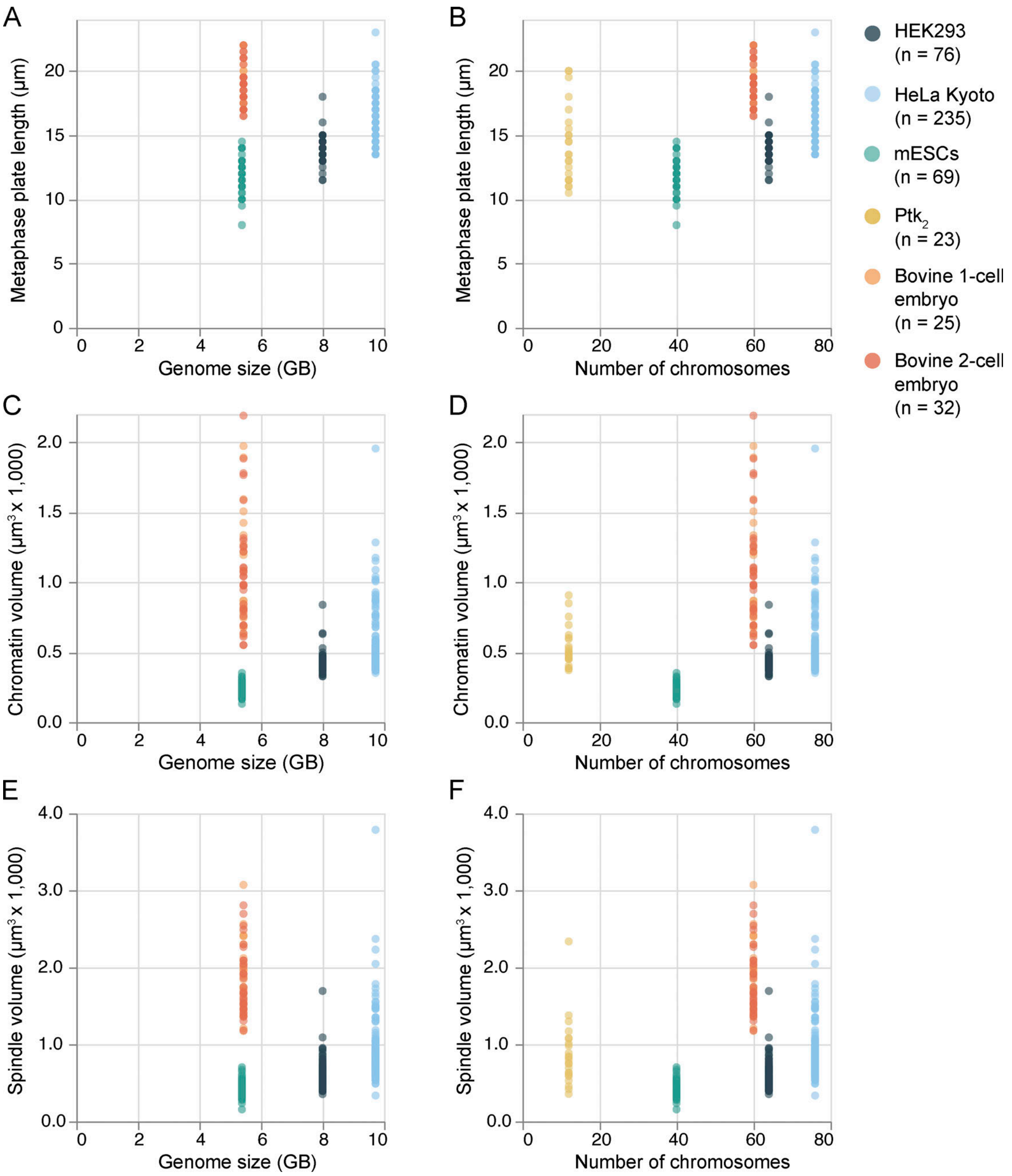

Figure S2. **Relationship between genome sizes and spindle and chromatin dimensions. (A and B)** Scatterplot displaying the relationship between genome size and metaphase plate length (A) and number of mitotic chromosomes and metaphase plate length (B). **(C and D)** Scatterplot displaying the relationship between genome size and chromatin volume (C) and number of mitotic chromosomes and chromatin volume (D). **(E and F)** Scatterplot displaying the relationship between genome size and spindle volume (E) and number of mitotic chromosomes and spindle volume (F). Circles represent single cells (HEK293, *n* = 76; HeLa Kyoto, *n* = 235; mESCs, *n* = 69; Ptk$_2$, *n* = 23; bovine one cell, *n* = 25; bovine two cell, *n* = 32). HEK293 cells were described as hypotriploid (3n−; Bylund et al., 2004) with an average chromosome number of 64. Considering the median human diploid genome size of 5.72 gigabytes (GB; NCBI) and the diploid human chromosome number of 46, we estimated the genome size to be ~8.00 GB. HeLa cells were described as hypertriploid (3n+; Macville et al., 1999) with an average chromosome number of 76; we estimated the average HeLa genome to be ~9.72 GB. The diploid genome of *M. musculus* corresponds to 40 chromosomes. The median diploid genome size is reported to be 5.38 Gb (NCBI). Analogously, the diploid genome of *B. taurus* corresponds to 60 chromosomes, the median diploid genome size is 5.44 GB (NCBI). The genome of the marsupial species *P. tridactylis* is not yet sequenced; the female diploid chromosome number is 12 (Rens et al., 1999).

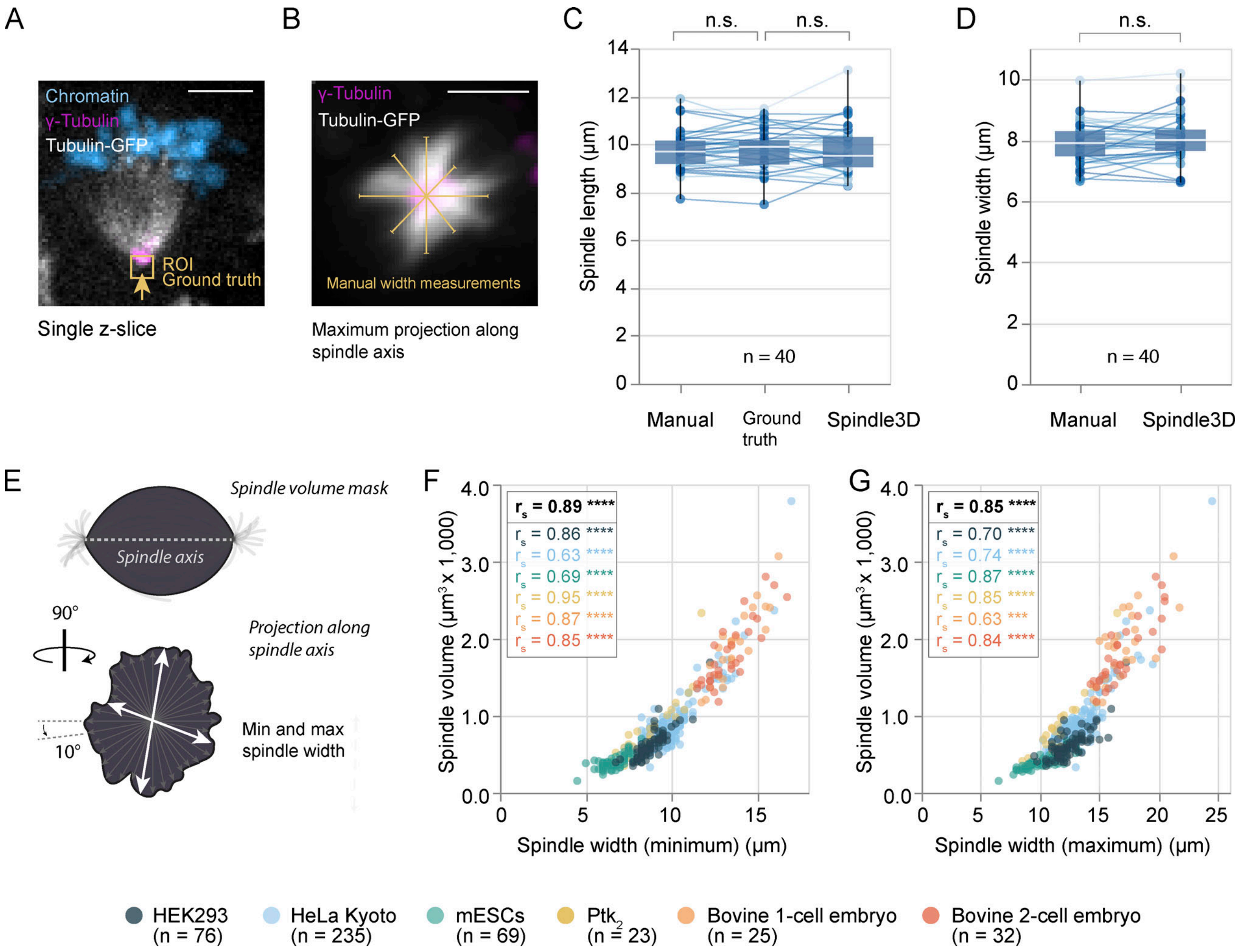

Figure S3. **Performance accuracy of manual versus automated spindle measurements. (A)** Micrograph (single z-slice) of a tubulin-GFP (grayscale) expressing mouse embryonic stem cell (mESC) fixed at mitosis. Antibody stainings were used to detect γ-tubulin (magenta). DNA is stained with Hoechst (blue). The arrow and region of interest (ROI; yellow) highlight the outer edge of the γ-tubulin signal, the position considered as ground-truth spindle pole. Scale bar, 5 µm. **(B)** Maximum projection along the spindle axis of a tubulin-GFP–expressing mitotic mESC with labeled centrosomes (γ-tubulin, magenta). Four manually drawn spindle width measurements (yellow) were averaged to yield the reference spindle width. Scale bar, 5 µm. **(C)** Box plots show distributions of spindle length measurements ($n = 40$) derived by manually placing spindle poles within the tubulin-only 3D image ("manual"), manually placing spindle poles within the γ-tubulin–only 3D image ("ground truth"), or subjecting the chromatin/tubulin stack to analysis by Spindle3D. **(D)** Box plots show distributions of spindle width measurements ($n = 40$) derived manually or via Spindle3D. Boxes reflect the interquartile range, and whiskers show the minimum and maximum. The medians are shown as horizontal white lines inside the boxes. Circles reflect measurements on individual spindles and are linked across the methods by lines. Hypothesis testing was performed using the Wilcoxon signed-rank test. n.s., $P > 0.05$. **(E)** Rationale for determining the minimum and maximum spindle width after segmentation in Spindle3D. **(F and G)** Scatterplots showing the relationship between the minimum spindle width and spindle volume (F) and between the maximum spindle width and spindle volume (G). Circles represent individual cells (HEK293, $n = 76$; HeLa Kyoto, $n = 235$; mESCs, $n = 69$; Ptk$_2$, $n = 23$; bovine one cell, $n = 25$; bovine two cell, $n = 32$). r_s, Spearman correlation coefficient. ***, $P < 0.001$; ****, $P < 0.0001$.

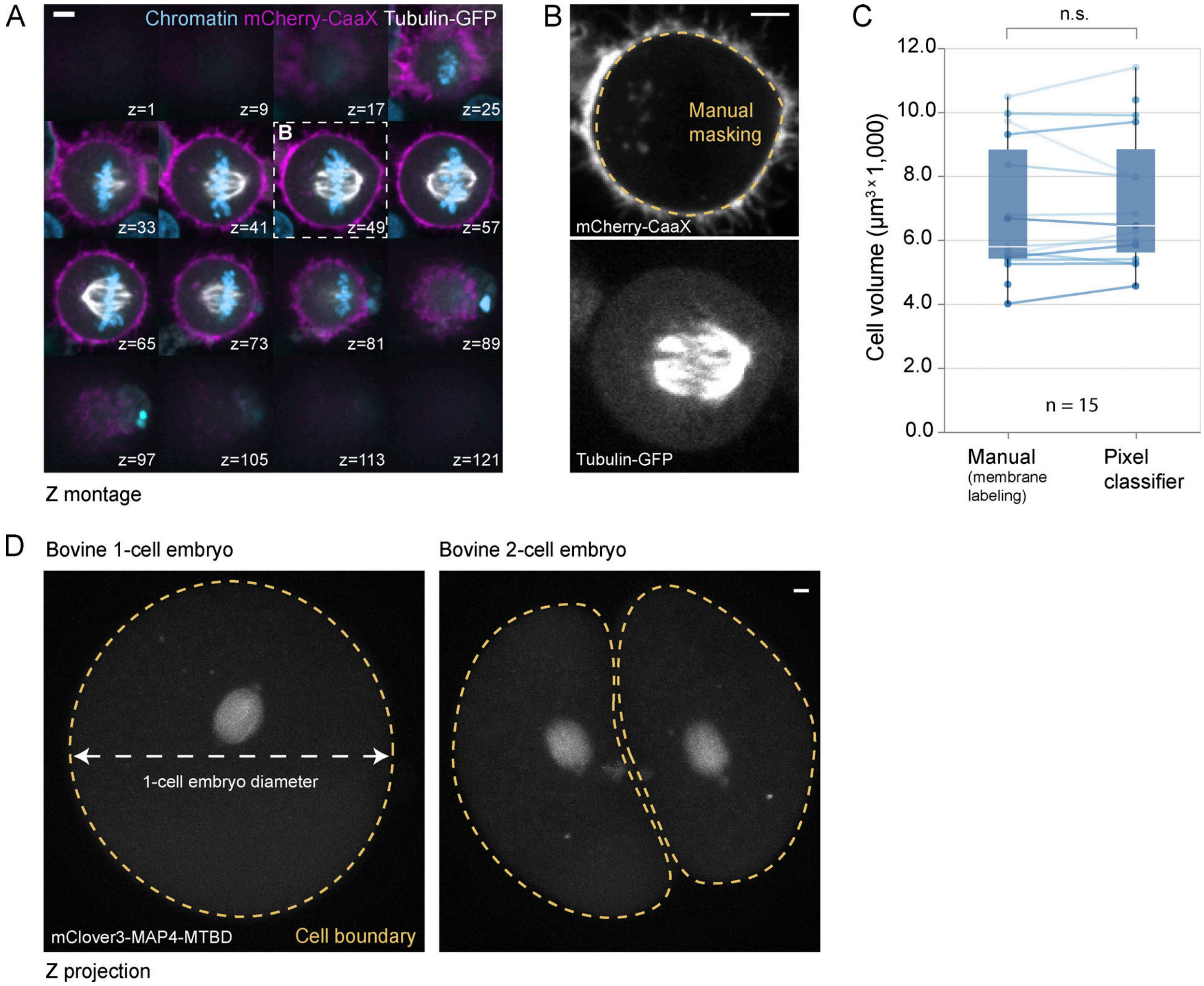

Figure S4. **Cell volume and diameter measurements. (A)** Z montage showing a mitotic HeLa Kyoto cell expressing tubulin-GFP (grayscale) and mCherry-CaaX (magenta); DNA (blue) was stained by SiR-DNA. Scale bar, 5 µm. **(B)** Isolated slice of A highlighting the cell membrane landmark channel (top) with the manually traced cell boundary (dashed line) and the tubulin-GFP channel (bottom) used in pixel classification–based segmentation. Scale bar, 5 µm. **(C)** Distributions showing cell volumes ($n = 15$) as determined in the landmark channels versus through pixel classification in the fluorescent tubulin channel. Boxes reflect the interquartile range, and whiskers show the minimum and maximum. The medians are shown as horizontal white lines inside the boxes. Circles reflect measurements on individual spindles and are linked across the methods by lines. Hypothesis testing was performed using the Wilcoxon signed-rank test. n.s., $P > 0.05$. **(D)** Z projections of a *B. taurus* embryo (expressing mClover3-MAP4-MTBD for the visualization of microtubules [grayscale]) at metaphase of the one-cell stage (left) or two-cell stage (right). Cell boundaries are highlighted with dashed yellow lines. The diameter of the one-cell embryo is indicated with a white dashed line. Scale bar, 5 µm.

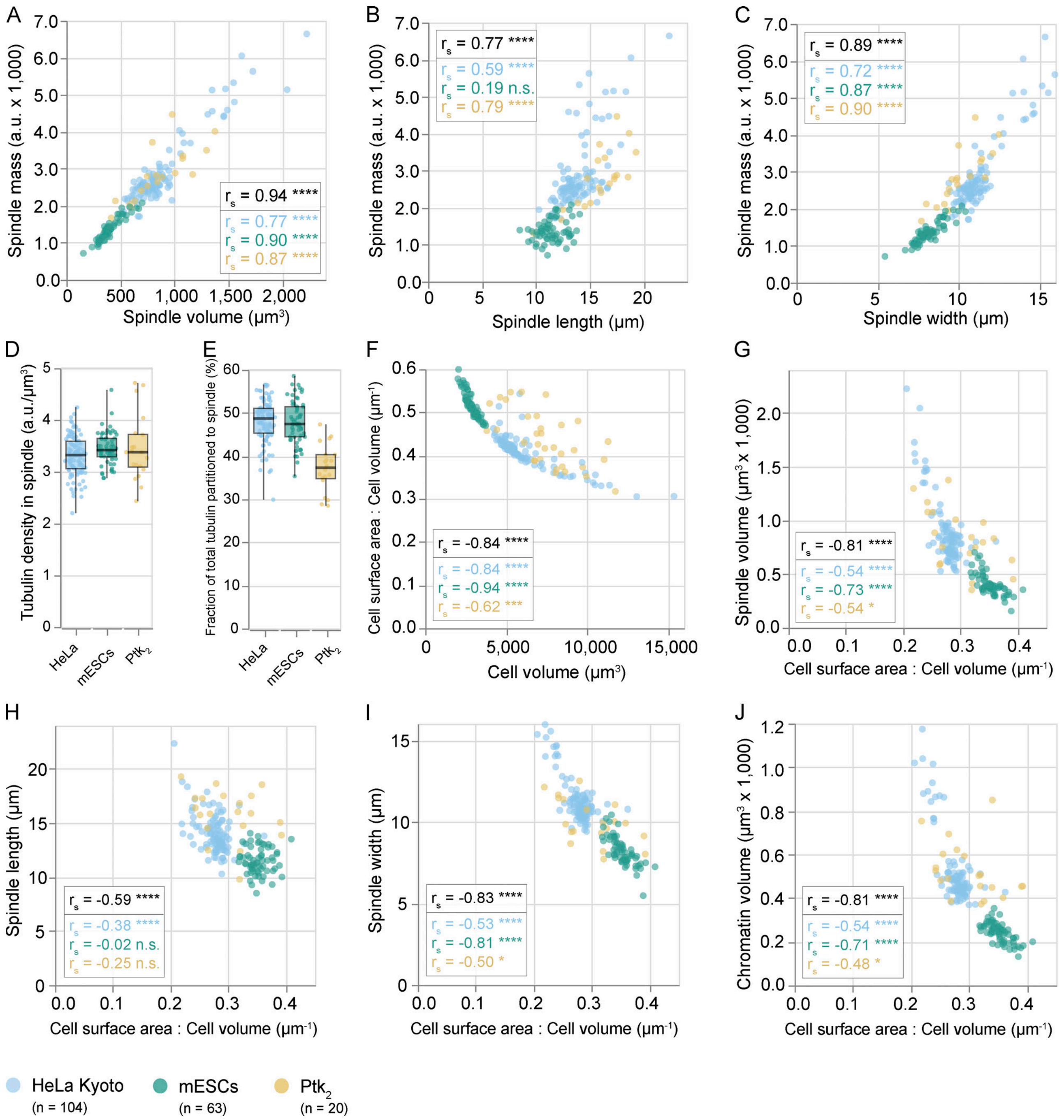

Figure S5. **CA/CV ratios do not explain the unique spindle scaling phenotype of Ptk$_2$ cells. (A–C)** Scatterplots displaying the relationship between spindle volume and spindle mass (A), between spindle length and spindle mass (B), and between spindle width and spindle mass (C). **(D and E)** Distributions of tubulin density in the spindle (polymer and free; D) and the fraction of total tubulin partitioned to the spindle (E). **(F)** Scatterplot showing the relationship between cell volume and CA/CV ratios in three cell types. **(G)** Spindle volume plotted against CA/CV. **(H–J)** Relationship between CA/CV ratio and spindle length (H), CA/CV ratio and spindle width (I), and CA/CV ratio and chromatin volume (J). Boxes reflect the interquartile range, and whiskers show the minimum and maximum. The medians are shown as horizontal white lines inside the boxes. Circles represent individual cells (HeLa Kyoto, *n* = 104; mESCs, *n* = 63; Ptk$_2$, *n* = 20). r_s: Spearman correlation coefficient. *, P < 0.05; ***, P < 0.001; ****, P < 0.0001; ns, P > 0.05.